Design of Continuously Reinforced Concrete Pavements Using Glass Fiber Reinforced Polymer Rebars

PUBLICATION NO. FHWA-HRT-05-081

OCTOBER 2005

U.S. Department of Transportation
Federal Highway Administration

Research, Development, and Technology
Turner-Fairbank Highway Research Center
6300 Georgetown Pike
McLean, VA 22101-2296

FOREWORD

This report, *Design of Continuously Reinforced Concrete Pavements Using Glass Fiber Reinforced Polymer Rebars,* investigates the effects on stress development in pavement and on critical design factors from substituting glass fiber reinforced polymer (GFRP) reinforcement for conventional steel reinforcement in continuously reinforced concrete pavements (CRCPs) in order to determine the performance characteristics of the GFRP-reinforced concrete pavements. The results of this study target the design of CRCPs with GFRP rebars as an applicable reinforcement and the proposal of feasible GFRP-CRCP designs to be constructed.

This report will be useful to those interested in the effect of GFRP reinforcing rebars on shrinkage and thermal stresses in concrete as studied using analytical and numerical methods as well as experimental measurements. This study proposes a series of designs for the GFRP-reinforced CRCP based on the numerical and mechanistic results, and reveals areas recommended for further investigation.

Gary L. Henderson
Director, Office of Infrastructure
Research and Development

Notice

Quality Assurance Statement

The Federal Highway Administration (FHWA) provides high-quality information to serve Government, industry, and the public in a manner that promotes public understanding. Standards and policies are used to ensure and maximize the quality, objectivity, utility, and integrity of its information. FHWA periodically reviews quality issues and adjusts its programs and processes to ensure continuous quality improvement.

1. Report No	2. Government Accession No.	3. Recipient's Catalog No.
FHWA-HRT-05-081	N/A	N/A

4. Title and Subtitle	5. Report Date
Design of Continuously Reinforced Concrete Pavements Using Glass Fiber Reinforced Polymer Rebars	October 2005
	6. Performing Organization Code: N/A

7. Authors(s)	8. Performing Organization Report No.
Jeong-Hoon Choi and Roger H. L. Chen, Ph.D.	N/A

9. Performing Organization Name and Address	10. Work Unit No. (TRAIS)
Department of Civil and Environmental Engineering West Virginia University Morgantown, WV 26506	N/A
	11. Contract or Grant No.: DTFH61-99-X-00078
	13. Type of Report and Period Covered: Final

12. Sponsoring Agency Name and Address	14. Sponsoring Agency Code
Office of Research and Technology Services Federal Highway Administration 6300 Georgetown Pike McLean, VA 22101	

15. Supplementary Notes

The Contracting Officer's Technical Representative on this contract was Peter Kopac, Pavement Materials and Construction Team.

16. Abstract

This is *Task 3: Continuously Reinforced Concrete Pavement*. The corrosion resistance characteristics of glass fiber reinforced polymer (GFRP) rebars make them a promising substitute for conventional steel reinforcing rebars in continuously reinforced concrete pavements (CRCPs). Studies are conducted on the effect of using GFRP rebars as reinforcement in CRCP on concrete stress development, which is directly related to the concrete crack formation that is inevitable in CRCP. Under restrained conditions, concrete volume change because of shrinkage and temperature variations is known to cause early-age cracks in CRCP. In this study, an analytical model has been developed to simulate the shrinkage and thermal stress distributions in concrete due to the restraint provided by GFRP rebars in comparison with the stresses induced by steel rebars. The results show that the stress level in concrete is reduced with GFRP rebars because of a low Young's modulus of GFRP. In addition, the analytical model has been used to estimate concrete strain variation in reinforced concrete slabs because of changes in concrete volume, and the results were compared with the experimental observation. Finite element (FE) methods are also developed to predict the stress distribution and crack width in the GFRP-reinforced CRCP section that is subjected to the concrete volume changes under various CRCP design considerations, such as the coefficient of thermal expansion (CTE) of concrete, the friction from the pavement's subbase, and the bond-slip between concrete and reinforcement. Based on the results from the FE simulation along with the mechanistic analysis, a series of feasible designs of the GFRP-reinforced CRCP is proposed. The stress levels in the GFRP reinforcement, the crack widths, and the crack spacings of the proposed pavements are shown to be within the allowable design requirements.

17. Key Words	18. Distribution Statement
GLASS FIBER REINFORCED POLYMER, CONTINUOUSLY REINFORCED CONCRETE PAVEMENTS, REBARS, CONCRETE STRESS	No restrictions. This document is available to the Public through the National Technical Information Service; Springfield, VA 22161

19. Security Classif. (of this report)	20. Security Classif. (of this page)	21. No. of Pages	22. Price
Unclassified	Unclassified	79	N/A

SI* (MODERN METRIC) CONVERSION FACTORS

APPROXIMATE CONVERSIONS TO SI UNITS

Symbol	When You Know	Multiply By	To Find	Symbol
		LENGTH		
in	inches	25.4	millimeters	mm
ft	feet	0.305	meters	m
yd	yards	0.914	meters	m
mi	miles	1.61	kilometers	km
		AREA		
in^2	square inches	645.2	square millimeters	mm^2
ft^2	square feet	0.093	square meters	m^2
yd^2	square yard	0.836	square meters	m^2
ac	acres	0.405	hectares	ha
mi^2	square miles	2.59	square kilometers	km^2
		VOLUME		
fl oz	fluid ounces	29.57	milliliters	mL
gal	gallons	3.785	liters	L
ft^3	cubic feet	0.028	cubic meters	m^3
yd^3	cubic yards	0.765	cubic meters	m^3
	NOTE: volumes greater than 1000 L shall be shown in m^3			
		MASS		
oz	ounces	28.35	grams	g
lb	pounds	0.454	kilograms	kg
T	short tons (2000 lb)	0.907	megagrams (or "metric ton")	Mg (or "t")
		TEMPERATURE (exact degrees)		
^oF	Fahrenheit	5 (F-32)/9 or (F-32)/1.8	Celsius	^oC
		ILLUMINATION		
fc	foot-candles	10.76	lux	lx
fl	foot-Lamberts	3.426	candela/m^2	cd/m^2
		FORCE and PRESSURE or STRESS		
lbf	poundforce	4.45	newtons	N
lbf/in^2	poundforce per square inch	6.89	kilopascals	kPa

APPROXIMATE CONVERSIONS FROM SI UNITS

Symbol	When You Know	Multiply By	To Find	Symbol
		LENGTH		
mm	millimeters	0.039	inches	in
m	meters	3.28	feet	ft
m	meters	1.09	yards	yd
km	kilometers	0.621	miles	mi
		AREA		
mm^2	square millimeters	0.0016	square inches	in^2
m^2	square meters	10.764	square feet	ft^2
m^2	square meters	1.195	square yards	yd^2
ha	hectares	2.47	acres	ac
km^2	square kilometers	0.386	square miles	mi^2
		VOLUME		
mL	milliliters	0.034	fluid ounces	fl oz
L	liters	0.264	gallons	gal
m^3	cubic meters	35.314	cubic feet	ft^3
m^3	cubic meters	1.307	cubic yards	yd^3
		MASS		
g	grams	0.035	ounces	oz
kg	kilograms	2.202	pounds	lb
Mg (or "t")	megagrams (or "metric ton")	1.103	short tons (2000 lb)	T
		TEMPERATURE (exact degrees)		
^oC	Celsius	1.8C+32	Fahrenheit	^oF
		ILLUMINATION		
lx	lux	0.0929	foot-candles	fc
cd/m^2	candela/m^2	0.2919	foot-Lamberts	fl
		FORCE and PRESSURE or STRESS		
N	newtons	0.225	poundforce	lbf
kPa	kilopascals	0.145	poundforce per square inch	lbf/in^2

*SI is the symbol for the International System of Units. Appropriate rounding should be made to comply with Section 4 of ASTM E380.
(Revised March 2003)

TABLE OF CONTENTS

LIST OF FIGURES

LIST OF TABLES

CHAPTER 1. INTRODUCTION

INTRODUCTION

Many distresses occurring in concrete structures are attributed to the corrosion of steel reinforcing rebars, a condition to which steel-reinforced continuously reinforced concrete pavement (CRCP) is typically subjected. According to a CRCP performance report, corrosion has been a major deteriorative factor for CRCPs in Wisconsin, causing delamination, spalling, and steel rupture.[1] Therefore, glass fiber reinforced polymer (GFRP) rebars—which are increasingly gaining attention for structural application because of their noncorrosiveness and high longitudinal strength, light self-weight, and nonmagnetic quality—can also be viable alternatives to steel reinforcing rebars for CRCP.

Conventional steel-reinforced CRCP has been built across the country since 1921, and its design can be found in a 1993 guide by the American Association of State Highway and Transportation Officials (AASHTO).[2] The behavior of conventional CRCP in response to concrete volume change has been well understood using mechanistic and numerical analysis methods, and its field performance has been monitored and analyzed as well; this has provided valuable information regarding some factors affecting the behavior and distresses deteriorating performance over time. (See references 1, 3, 4, and 5.) However, since little research concerning the replacement of steel reinforcing rebars with GFRP rebars in CRCP has been conducted, initial studies of mechanical behavior and design considerations for GFRP-reinforced CRCP need to be completed prior to any field application.

At the onset of this study, the effects of using GFRP reinforcing rebars on shrinkage and thermal stress development in concrete were investigated. Shrinkage and thermal stresses in concrete have been known to cause incipient cracking in CRCPs or bridge decks. In order to optimally control concrete cracking (which has a strong influence on the performance and longevity of such structures), it is important to understand the development of these stresses in the structures. In the case of a freely supported reinforced concrete slab subjected to shrinkage or temperature variation, concrete stresses result from the restraint provided by the reinforcement. While concrete shrinkage causes tensile stresses in concrete, temperature variation can cause either tensile or compressive stresses in concrete, depending on whether the temperatures drop or rise and on the way of combining the coefficients of thermal expansion (CTEs) of the concrete and the reinforcement used.[6,7] The CTE of concrete varies primarily with the type of coarse aggregate used, and the CTE of the GFRP depends on the types of fibers and resins and the volume fraction of fiber used. In the case of slab on ground or bridge decks, however, other restraining forces acting on the concrete slab—such as friction from the subbase under concrete pavements, restraints from the girders underneath bridge decks, or restraints from reinforcement ties to neighboring slabs—need to be considered. When these restraints are considered, the overall resulting stress in the concrete will differ from that for a freely supported concrete slab (mostly by having a higher tensile stress level).

In this report, analytical studies for a freely supported reinforced concrete slab are first presented to describe the effect of GFRP reinforcing rebars on shrinkage and thermal stresses in concrete, and the results are compared with the experimental measurements. A finite element (FE) model for the freely supported reinforced concrete slab was developed, and the results were verified by the analytical results. FE analyses were also conducted for the GFRP-reinforced CRCPs; transverse cracks were spaced at 1.524 meters (m) (5 feet (ft)), which are subjected to both concrete shrinkage and temperature change. In the FE analyses, various CRCP design considerations (such as the CTE of concrete, the friction from the pavement's subbase, and the bond-slip between concrete and reinforcement) were studied to understand their effects on stress development and crack width in the CRCP; additional effects of crack spacing were studied using CRCP slab segments of lengths 1.067 meters (m) (3.5 feet (ft)), 1.524 m (5 ft), and 2.438 m (8 ft).[8,9]

The FE analysis has also been employed to create a feasible longitudinal reinforcement design for a 25.4-centimeter- (cm-) (10-inch-) thick GFRP-reinforced CRCP as an example. Using number 6 GFRP rebars at 15-cm (6-inch) spacing at the middepth of the slab is shown to be an economically feasible design for GFRP-CRCP on a flexible subbase (or lime-treated clay subbase). Although a larger amount of GFRP reinforcement is sometimes required to satisfy the allowable crack spacing (1.067 to 2.438 m (3.5 to 8 ft)), crack width (≤1 millimeter (mm) (0.04 inch)), and reinforcement stress level (20 percent of GFRP ultimate tensile strength) comparable to those from number 6 steel rebars at a 15.24-cm (6-inch) spacing at the middepth, the proposed design for GFRP-CRCP has been further examined using a mechanistic analysis program, CRCP8, and proven to perform satisfactorily for given material properties and design conditions provided by the Virginia Department of Transportation (VDOT). Other feasible designs for the given condition were also investigated, considering the effects of concrete coarse aggregate and subbase types on the development of crack by the mechanistic analysis.

OBJECTIVE AND SCOPE

The objective of this study is to investigate the effects on stress development in pavement and on critical design factors from substituting GFRP reinforcement for conventional steel reinforcement in CRCPs to determine the performance characteristics of the GFRP-reinforced concrete pavements. The results of this study target the design of CRCP with GFRP rebars as an applicable reinforcement and propose feasible GFRP-CRCP designs to be constructed.

The scope of this report includes studying the effect of GFRP reinforcing rebars on shrinkage and thermal stresses in concrete by analytical and numerical methods as well as by experimental measurements, and proposing a series of designs for the GFRP-reinforced CRCP based on the numerical and mechanistic results. The study also reveals some areas where further studies are recommended.

CHAPTER 2. LITERATURE REVIEW

CONTINUOUSLY REINFORCED CONCRETE PAVEMENT (CRCP)

General

CRCP is a type of Portland cement concrete pavement reinforced with steel rebars throughout its length. The first CRCP was constructed in 1921 on Columbia Pike near Washington, D.C., for experimental purposes, and by the 1940s and 1950s many states began conducting extensive studies on the effects of various designs and construction factors on its performance.[10] The extensive use of CRCP began in the early 1960s during the heyday of the Interstate System construction program, and there are now over 45,080 lane kilometers (km) (28,000 lane miles (mi)) of CRCP constructed in the United States throughout more than 35 states.[11] The use of continuous reinforcement generates the random cracks in the pavement, while obviating the need for transverse contraction joints that appear prone to joint-related distresses and failures. The cracks can be held tightly by the reinforcement and should be of no concern so long as they are uniformly spaced, maintaining the structural integrity of the pavement. Figure 1 shows the longitudinal steel rebars made continuous and the transverse steel rebars supporting the longitudinal rebars.[12]

Figure 1. Photo. Typical example of reinforcement layout for CRCP (constructed on S.R. 288 in Virginia).[12]

The high durability and strength characteristics of CRCP, obtained through its unique design, assure its longevity and low-maintenance cost, and will provide an excellent support for future overlays. Also, the elimination of transverse contraction joints can offer high riding quality. In order to realize such a level of benefit, the CRCP needs to be designed and constructed properly. Otherwise, premature failure will occur when it is subjected to ever-increasing heavy traffic loading.[13] The design and construction features that considerably affect the performance of CRCP are reinforcement ratio, pavement thickness, concrete material properties decided by coarse aggregate type, water-to-cement ratio, chemo-thermo-mechanical behavior, subbase quality and drainage, and reinforcement placement. (See references 1, 14, 15, and 16.) A study indicated that many examples of CRCP over 50 years old were still in serviceable condition and were able to carry traffic loads in excess of their projected design loadings, possessing low-maintenance cost and good riding quality.[16]

The distress most prevalent in CRCP is punchout failure at the pavement edge. There are four types and causes of distresses that commonly occur in CRCP:

- "Pumping" is the ejection of base or subgrade materials by water through a crack caused by the deflection of slab under moving loads. This results in a progressive loss of pavement support. The upward warp and curl of the slab near cracks due to a gradient of concrete volume change contribute to the pumping condition.

- "Faulting" is a difference of slab elevation across a crack. Faulting is caused by a buildup of loose materials under the trailing slab near the crack as well as at the depression of the leading slab. The buildup is caused by pumping due to heavy loading, and lack of load transfer contributes greatly to faulting.

- "Spalling" of cracks is the cracking, breaking, or chipping of the slab edges within 0.610 m (2 ft) of the crack. Spalling usually results from excessive stresses at the crack caused by infiltration of incompressible materials and subsequent expansion or traffic loading. It can also be caused by the disintegrated and weakened concrete at the crack caused by the reinforcement excessively stressed in tension.

- "Punchout" is the major structural distress of CRCP. When the concrete slab cracks, the tensile stress in the reinforcement causes the fracture of surrounding concrete near the crack. The fracture of concrete reduces the stiffness of the slab and results in spalling on the crack surface under continuous traffic loadings, which consequently makes the crack open wide and results in the loss of load transfer across the crack. Without the load transfer, the slab between two closely spaced cracks, usually less than 0.610 m (2 ft) apart, acts as a cantilever beam, and as the applications of heavy truck load continue, a short, longitudinal crack forms between the two transverse cracks about 0.610 to 1.524 m (2 to 5 ft) from the pavement edge.[10]

Loss of subbase support is the fundamental cause of all the distresses. Instances where nonuniform support has precipitated localized short crack spacing, leading ultimately to

punchout failure, have been reported in one study.[14] An optimum crack spacing between 0.914 and 1.219 m (3 to 4 ft) was indicated because the maximum longitudinal and transverse bending stresses are minimized in terms of load transfer.[14] Maintaining high load transfer is critical to CRCP performance, particularly outside of this cracking interval, and is highly dependent on the crack width.[17] The other possible distresses are corrosion of steel reinforcement, blowup at transverse construction joint, and D-cracking adjacent and roughly parallel to cracks as well as along the slab edge.[1,10,18] The corrosion of steel reinforcement also leads to delamination, spalling, and steel rupture.

AASHTO Design Guide and Limiting Criteria for CRCP

The design for CRCP is based on empirical equations obtained from the AASHTO Road Test, and further modifications are based on theory and experience.[10] In the AASHTO design method, the procedure for determining the thickness of CRCP is the same as that used for conventional jointed pavement. The only difference in thickness design between the methods is that a slightly smaller load transfer coefficient (which implies more load transfer across the cracks) is used for CRCP, causing the thickness of the CRCP slab to be slightly smaller. However, according to a Portland Cement Association (PCA) report, the critical stresses and deflections in CRCP were about the same as those in conventional pavements, sometimes slightly larger and sometimes slightly smaller depending on the crack spacing, so the use of the same thickness has been recommended.[10, 19]

The AASHTO method for designing longitudinal reinforcement utilizes the nomographs developed by empirical equations. The input variables used for the design are concrete tensile strength, concrete shrinkage, CTE of concrete and steel rebar, rebar diameter, design temperature drop, and wheel load tensile stress. In addition, there are three limiting criteria which must be considered for the design: crack spacing, crack width, and reinforcement stress. The acceptable limits of these criteria (summarized below) can ensure satisfactory performance of CRCP under the anticipated environmental and vehicular loading conditions:[2]

- Crack spacing: The limits on crack spacing are established in consideration of spalling and punchout. To minimize crack spalling, the maximum spacing between consecutive cracks should be no more than 2.438 m (8 ft), whereas to minimize the potential for punchout, the minimum desirable spacing is 1.067 m (3.5 ft).

- Crack width: The limit on crack width is based on a consideration of spalling and water penetration. The allowable crack width should not exceed 1 mm (0.04 inch). The crack width should be reduced as much as possible through the selection of a higher steel percentage or smaller diameter reinforcing rebars.

- Reinforcement stress: Limiting criteria on reinforcement stress is intended to guard against steel fracture and excessive permanent deformation. To avoid these, a limiting stress of 75 percent of the ultimate tensile strength of steel rebar is recommended.

The steel reinforcement ratio adopted varies from region to region. By far, the most commonly used amount of steel reinforcement is 0.6 percent. Under more severe weather conditions, 0.7 percent of steel amount is preferable.[1,3,20]

Review of Mechanistic Analysis Program Development

In 1974, researchers at the University of Texas developed their first computer program for the mechanistic analysis of CRCP. Extensive field studies conducted to verify the validity of the program (CRCP1) indicated that the predictions from CRCP1 agreed with field observations. The effect of wheel load stresses was added to the CRCP behavior due to environmental loading, and the CRCP program was continuously improved by simulating material variance to concrete tensile strength and adding fatigue failure models.[3] Normalized concrete curing curves were determined for various coarse aggregates commonly used in Texas, and these curves and the calibrated failure prediction model were included.[5,21] Finally, all previous versions of the CRCP programs were integrated into one program (CRCP8) for simplification of the user input process.[22] However, CRCP8 still had some limitations spawning from the simplified assumption of the one-dimensional analysis. In 1998, a new program, CRCP9 (which uses two-dimensional finite element theories to create a mechanistic model) was developed.[4] The CRCP9 includes consideration of nonlinear variation in temperature and drying shrinkage through the depth of a concrete slab, the nonlinear bond-slip relationship between concrete and steel rebars, viscoelastic effects of concrete, curling and warping effects, and the ability to change locations of the longitudinal reinforcement. To improve the accuracy of the wheel load stress calculation, the program was updated once again by including the effect of the moving dynamic tandem axle loads (CRCP10).[23]

FIBER REINFORCED POLYMER (FRP) REINFORCEMENT

Steel reinforcement has been widely used for conventional concrete structure. In general, steel reinforcement is chemically protected by the high alkalinity (pH 12.5 to 13.5) of the concrete and physically protected by surrounding concrete cover against corrosion.[24] However, for many structures exposed to aggressive environments (such as marine structures, bridges, loads, and parking garages), combinations of moisture, temperature, and chlorides reduce the alkalinity of the concrete and result in the corrosion of steel reinforcement. The corrosion process of steel reinforcement leads to concrete deterioration followed by the eventual loss of structural serviceability. To overcome corrosion problems, researchers have examined numerous options that can prevent corrosive agents from reaching the steel reinforcement surface, such as applications of epoxy coating and cathodic protection to the steel reinforcement, the use of sealers and membranes, lower permeability concrete, and corrosion-inhibiting chemical admixtures.[25] However, the potential of corrosion problems still remains with the constant presence of corrosive agents, and therefore the effectiveness of these options may vary considerably in the long run.

In recent efforts to solve the corrosion problems in concrete, nonmetallic materials such as fiber reinforced polymer (FRP) composites have become an alternative to reinforcing

steel in various concrete structures. FRP reinforcement is primarily made of fibers embedded in a polymeric resin. The small diameter inorganic and organic fibers (e.g., glass, carbon, aramid, and polyvinyl alcohol) provide FRP reinforcement with strength and stiffness, whereas thermosetting polymer resins (e.g., polyester, vinylester, and epoxy) bind the fibers together. In addition, inorganic fillers (e.g., calcium carbonate, clay, and alumina trihydrate) can be mixed with the resins for cost reduction, property modification, and processing property control of FRP reinforcement.

The FRP reinforcement has some advantages and disadvantages in its material characteristics when used in concrete structures:[26]

- Advantages
  - High longitudinal strength.
  - Nonmagnetic.
  - Corrosion resistance.
  - High fatigue endurance.
  - Light weight (about one-fifth to one-fourth the density of steel).
  - Low thermal and electric conductivity.

- Disadvantages
  - High cost.
  - No yielding before brittle rupture.
  - Low transverse strength.
  - Low modulus of elasticity.
  - Susceptibility to damage due to ultra-violet radiation.
  - Low durability of glass fibers in a moist environment.
  - Low durability of some glass and aramid fibers in an alkaline environment.
  - High CTE perpendicular to the fibers, relative to concrete.
  - Susceptibility to fire, depending on matrix type and concrete cover.

Therefore, the material characteristics of FRP need to be carefully considered when determining whether FRP reinforcement is suitable or necessary for a particular concrete structure. There are several commercially available FRP reinforcements made of continuous aramid (AFRP), carbon (CFRP) or glass (GFRP) fibers embedded in various resin materials. Also, FRP reinforcements can be sorted by the type of surface deformation system, such as exterior wound fibers, sand coating, or separately formed deformation.

Currently, the structural performance and integrity of concrete structures reinforced with FRP rebars are being studied extensively by researchers in Japan, Europe, and North America in order to investigate FRP rebar structure capability and durability as reinforcement for concrete and to provide FRP design provisions for different applications. A preliminary design method of FRP reinforcement for jointed slabs on the ground is presented in an ACI committee report.[26] The subgrade drag method is

frequently used to determine the amount of shrinkage and temperature steel reinforcement as:

$$A_s = \frac{\mu L w}{2 f_s}$$

Figure 2. Equation. A_s.

where A_s = cross-sectional area of steel (in^2) per linear foot; f_s = allowable stress in steel reinforcement (lbf/in^2), commonly taken as two-thirds to three-fourths of yielding stress level; μ = coefficient of subgrade friction (1.5 is recommended for floors on ground); L = distance between joints (ft); and w = dead weight of the slab (lbf/ft^2) per slab thickness. The drag equation is modified by considering the lower modulus of the FRP reinforcement. At the allowable stress, the strain in steel reinforcement is about 0.0012, and converting the same strain into the stress for FRP will give a stress of $0.0012E_f$. Figure 2 can then be rewritten as:

$$A_{f,sh} = \frac{\mu L w}{2(0.0012 E_f)}$$

Figure 3. Equation. $A_{f,sh}$.

where $A_{f,sh}$ = the cross-sectional area of FRP reinforcement (in^2) per linear foot; and E_f = Young's modulus of FRP reinforcement (lbf/in^2). Comparing figures 2 and 3, it can be noted that the ratio of the amount of FRP reinforcement required to be increased is the same as the ratio of steel to the GFRP Young's modulus. However, according to the ACI report, this design approach still needs to be experimentally verified. More importantly, there is a need to consider the effects due to the difference in CTE and Young's modulus between concrete and the types of reinforcement. An analytical study to address these effects will be presented in the next chapter.

CHAPTER 3. ANALYTICAL STUDY

ANALYTICAL MODEL FOR FREELY SUPPORTED REINFORCED CONCRETE SLAB

To estimate the development of shrinkage and thermal stresses in a freely supported reinforced concrete slab, a representative concrete prismatic model containing a longitudinal reinforcing rebar at its center with width (or reinforcing space in CRCP) B, height (or thickness in CRCP) H, length L, and rebar diameter $2r_r$ is considered. Then, for simplification of analysis, the model is modified into an equivalent cylinder with the corresponding equivalent diameter $2R$ accompanied by the same length and rebar diameter as those for the prismatic model. Schematic details of the models are shown in figures 5 and 6.

$$R = \sqrt{\frac{HB}{\pi}}$$

Figure 4. Equation. *R*.

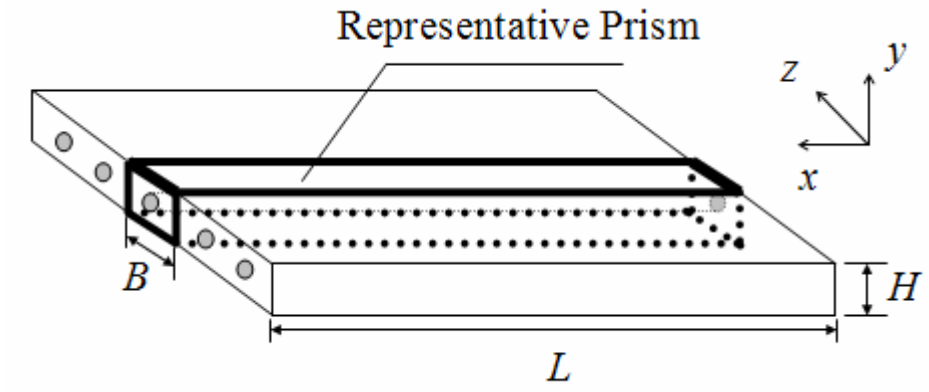

Figure 5. Drawing. Schematic details of representative reinforced concrete prism.

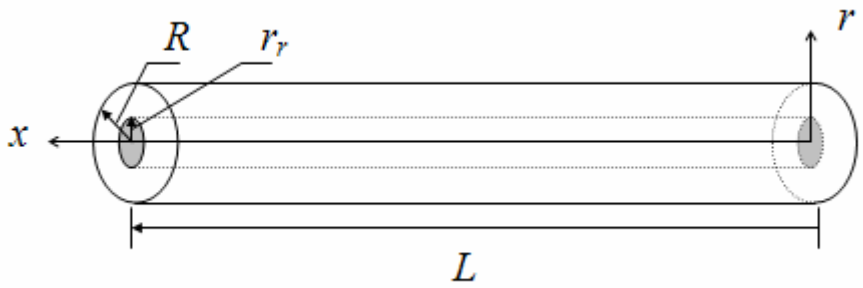

Figure 6. Drawing. Schematic details of equivalent cylinder used in analyses.

Adopting the shear-lag theory, there are several assumptions applied to this analysis: (1) the concrete and reinforcement exhibit elastic behavior, (2) a perfect bond between concrete and reinforcement exists at an infinitely thin interface, (3) the stiffnesses of the concrete and the reinforcement in the radial (*r*-) direction are the same, (4) the strain in the concrete ε_c at a distance *R* from the *x*-axis is equivalent to the restraint-free concrete strain due to the shrinkage or temperature variation, and (5) the temperature distribution in the concrete and reinforcement is uniform in the radial direction.[27] The effects of concrete's radial shrinkage on concrete stress development in the longitudinal (*x*-) direction are neglected. Also, the effects from the CTE discrepancies between concrete and reinforcement in the radial direction are neglected.

When the concrete is subjected to a strain in the longitudinal (*x*-) direction, ε_c, the rate of transfer of load from concrete to reinforcement can be assumed as:

$$\frac{dP}{dx} = C_o(u - v)$$

Figure 7. Equation. *dP/dx*.

where *P* = load in the reinforcement; C_o = a constant; and *v* and *u* = axial displacements at $r = R$ and $r = r_r$, respectively. It is also known from force equilibrium that $dP/dx = 2\pi r\tau$, where τ is the axial shear stress varying along the radial direction. This gives:

$$\tau(r) = \frac{dP}{dx}\frac{1}{2\pi r}$$

Figure 8. Equation. *τ(r)*.

The relative displacement between *u* and *v* can be obtained by:

$$(u-v)=\int_{r_r}^{R}\gamma(r)\,dr=\int_{r_r}^{R}\frac{\tau(r)}{G_c}\,dr$$

Figure 9. Equation. *(u-v)* in the form of integrating γ(r).

where $\gamma(r)$ = axial shear strain varying along the radial direction; and G_c = shear modulus of concrete. By solving figure 9, one then gets:

$$(u-v)=\frac{dP}{dx}\frac{\ln(R/r_r)}{2\pi G_c}$$

Figure 10. Equation. *(u-v)* in the solved form.

Hence,

$$C_o=\frac{2\pi G_c}{\ln(R/r_r)}$$

Figure 11. Equation. C_o.

Also, $dv/dx = \varepsilon_c$ and $du/dx = \varepsilon_r$. Therefore,

$$\frac{d^2P}{dx^2}=C_o(\varepsilon_r-\varepsilon_c)$$

Figure 12. Equation. d^2P/dx^2.

The restraint-free concrete axial strain, ε_c, in the above equation can be substituted with either shrinkage strain at any time *t* (in days (d)), $\varepsilon_{c,s}(t)$, or thermal strain, $\varepsilon_{c,t}$, which are given by:

$$\varepsilon_{c,s}(t)=\frac{-t}{35+t}(\varepsilon_{c,s})_{ult}$$

Figure 13. Equation. $\varepsilon_{c,s}(t)$.

and

$$\varepsilon_{c,t}=\Delta T\alpha_c$$

Figure 14. Equation. $\varepsilon_{c,t}$.

where $(\varepsilon_{c,s})_{ult}$ = ultimate shrinkage strain for drying at 40 percent RH; ΔT = temperature variation; and α_c = CTE of concrete. $\varepsilon_{c,s}(t)$ is an empirical equation for moist cured concrete.[28] The reinforcement axial strains due to concrete shrinkage, $\varepsilon_{r,s}$, or due to temperature variation, $\varepsilon_{r,t}$, are shown as:

$$\varepsilon_{r,s} = \frac{P}{A_r E_r}$$

Figure 15. Equation. $\varepsilon_{r,s}$.

and

$$\varepsilon_{r,t} = \Delta T \alpha_r + \frac{P}{A_r E_r}$$

Figure 16. Equation. $\varepsilon_{r,t}$.

where A_r = reinforcement cross-sectional area; E_r = Young's modulus of the reinforcement; and α_r = CTE of the reinforcement.

Substituting figures 13–16 into figure 12 gives the governing differential equation for P, and then by solving the differential equation with the boundary conditions that $P = 0$ at $x = 0$ and $x = L$, the reinforcement force, $P(x)$, can be obtained. The axial force equilibrium with the average axial concrete stress, $(\sigma_c)_{avg}$, must also be satisfied at any x location. In other words, $P + (\sigma_c)_{avg} A_c = 0$, where A_c is the concrete cross-sectional area. Hence, the average axial concrete stress can be given as follows:

$$(\sigma_{c,s})_{avg} = \rho E_r \frac{t}{35+t} (\varepsilon_{c,s})_{ult} \left[1 - \frac{\cosh \beta \left(\frac{L}{2} - x \right)}{\cosh \beta \frac{L}{2}} \right]$$

Figure 17. Equation. $(\sigma_{c,s})_{avg}$.

and

$$(\sigma_{c,t})_{avg} = -\rho E_r \Delta T (\alpha_c - \alpha_r) \left[1 - \frac{\cosh \beta \left(\frac{L}{2} - x \right)}{\cosh \beta \frac{L}{2}} \right]$$

Figure 18. Equation. $(\sigma_{c,t})_{avg}$.

where $(\sigma_{c,s})_{avg}$ and $(\sigma_{c,t})_{avg}$ = average axial concrete stresses induced by concrete shrinkage and temperature variation, respectively; ρ = reinforcing ratio (A_r/A_c); and

$$\beta = \sqrt{\frac{2G_c / E_r}{r_r^2 \ln(R / r_r)}}$$

Figure 19. Equation. β.

The negative values from figures 17 and 18 indicate compressive axial stresses in the concrete. The maximum axial stress in concrete can be simply found at the midpoint, $x = L/2$.

MATERIAL PARAMETERS FOR ANALYTICAL APPROXIMATION

In addition to the concrete shrinkage strain, $\varepsilon_{c,s}(t)$, shown in figure 13, the Young's modulus of concrete, E_c, is also employed as the time-dependent parameter in the shrinkage stress analysis. This leads the shrinkage stress analysis to be dependent on the elapsed time, t (d). The time-dependent Young's modulus of concrete can be evaluated by:

$$E_c(t) = E_{c,28}[0.52 + 0.15\ln(t)] \qquad \text{for } t \le 28$$

Figure 20. Equation. $E_c(t)$.

and

$$E_c = 1.019E_{c,28} \qquad \text{for } t > 28$$

Figure 21. Equation. E_c.

where $E_{c,28}$ = Young's modulus of concrete at 28 d.[29] In the thermal stress analysis, the concrete stresses at 28 d are estimated for different temperature variations; $E_{c,28}$ was therefore employed for the Young's modulus of concrete in the analysis. Table 1 lists a set of model parameters and material properties used in the analytical study. The analytical model with a width of B = 15.24 cm (6 inches) and a height of H = 25.4 cm (10 inches) was examined in the study. Shown in the table are the Young's moduli and CTEs of two different concretes whose types of coarse aggregate used are granite and siliceous river gravel, respectively.[30] In addition, the GFRP rebar used in the analyses is assumed to be C-BAR® deformed FRP rebar, manufactured by Marshall Industry Composite, Inc.

ANALYTICAL RESULTS AND DISCUSSION

In figure 22, the maximum average tensile stresses in the concrete due to concrete shrinkage are calculated over a period of time; the stresses induced by steel and GFRP

reinforcements are shown in the figure for the purpose of comparison, and the granite aggregate concrete is used in the shrinkage stress analysis. In the calculation, number 5 rebars with radii of 7.94 mm (0.3125 inch; $\rho = 0.00519$) are employed for the models having a length of $L = 1.524$ m (60 inches (5 ft)). The figure reveals that the maximum concrete stress level created by GFRP rebar is about one-fifth of that created by steel rebar, which is a ratio about the same as that of the longitudinal GFRP rebar's elastic modulus to the steel rebar's elastic modulus. The lower stress level by GFRP rebar results from the GFRP's lower elastic modulus providing the concrete with less restraint while the concrete shrinks.

Table 1. Model parameters and material properties used in analytical approximation.

Parameter and Properties	Value
Width, B (cm (inches))	15.24 (6.0)
Height, H (cm (inches))	25.40 (10.0)
Length, L (m (inches))	1.52 (60.0)
Ultimate concrete shrinkage strain, $(\varepsilon_{c,s})_{ult}$ ($\mu\varepsilon$)	800.00
Young's modulus of concrete at 28 d, $E_{c,28}$ (GPa (× 10^6 lbf/in^2))	33.10 (4.80)[1] and 34.48 (5.0)[2]
Poisson's ratio of concrete, ν_c	0.20
Young's modulus of steel rebar (GPa (× 10^6 lbf/in^2))	200.00 (29.00)
Longitudinal Young's modulus of GFRP rebar (GPa (× 10^6 lbf/in^2))	40.00 (5.80)
CTE of concrete, α_c ($\mu\varepsilon$/°C ($\mu\varepsilon$/°F))	10.26 (5.7)[1] and 14.40 (8.0)[2]
CTE of steel rebar, $\alpha_{r,s}$ ($\mu\varepsilon$/°C ($\mu\varepsilon$/°F))	11.88 (6.6)
CTE of GFRP rebar, $\alpha_{r,g}$ ($\mu\varepsilon$/°C ($\mu\varepsilon$/°F))	9.36 (5.2)

[1]Granite coarse aggregate.
[2]Siliceous river gravel coarse aggregate used.
1 megapoundforce per square inch (10^6 lbf/in^2) = 6.89 gigapascal (GPa)

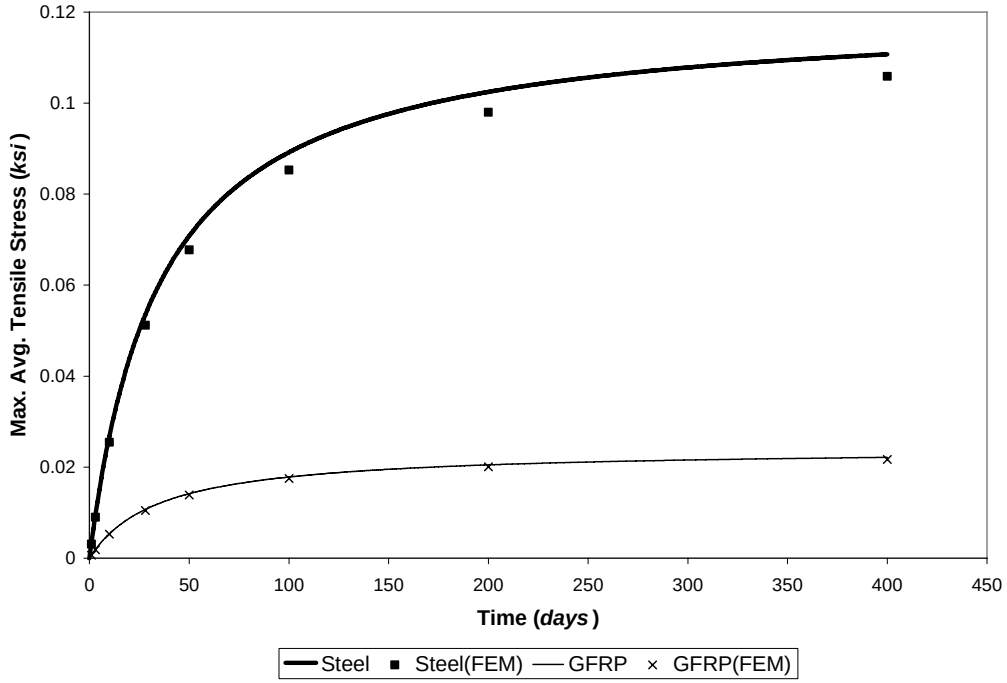

1 kilopoundforce per square inch (ksi) = 6.89 megapascal (MPa)

Figure 22. Graph. Maximum average tensile stress in concrete versus time (ρ = 0.00519 and L = 1.524 m (60 inches)).

The cases for different sizes of GFRP rebars (numbers 3 through 6 (ρ = 0.00184 through 0.00739)) are presented in figure 23, showing that the maximum concrete stress increases with an increase in the reinforcement ratio. This is because of the greater restraint provided to the concrete shrinkage by a higher reinforcement ratio. The maximum concrete stresses for different slab lengths, L, are examined in figure 24. The stresses increase with increases in length, L, increasingly converging to $\rho E_r \varepsilon_{c,s}(t)$ when L approaches ∞. With the set of parameters (table 1) used, the maximum concrete stress already converges to $\rho E_r \varepsilon_{c,s}(t)$ as L reaches about 0.305 m (12 inches).

The discrepancy in CTEs between the concrete and reinforcement causes thermal stresses in both the concrete and reinforcement as temperatures change. Figures 23 and 24 show the plots of the maximum average axial stress in concrete versus temperature increase (positive ΔT) for two different concrete CTEs. The CTE of granite aggregate concrete is lower than that of steel rebar and higher than that of GFRP rebar (table 1). As shown in figure 25, this CTE of concrete causes tensile concrete stress when using steel rebar and compressive concrete stress when using GFRP rebar as temperature increases; in the figure, the positive value represents the tensile stress, and the negative value the compressive stress.

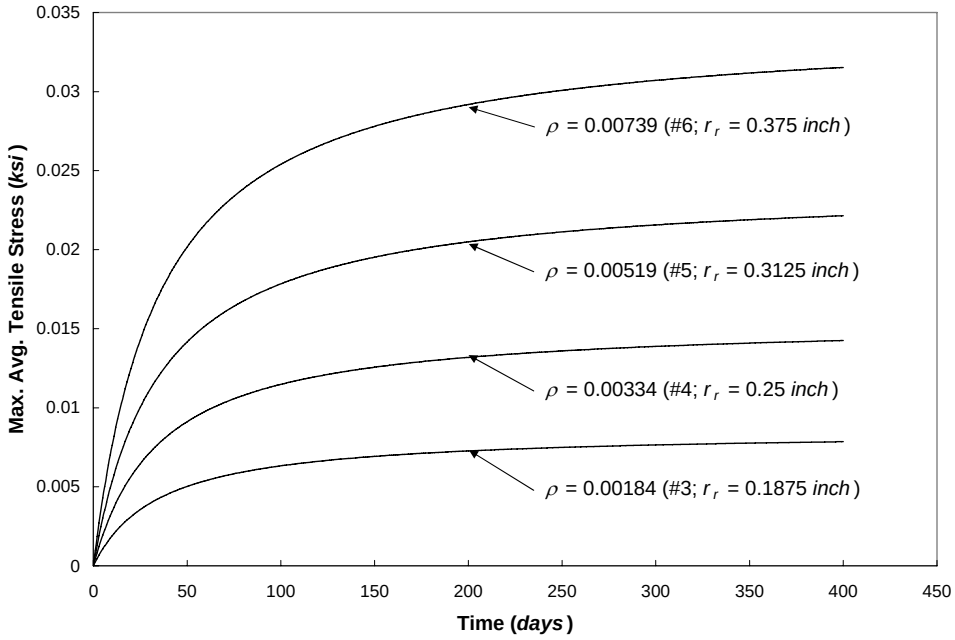

1 ksi = 6.89 MPa; 1 inch = 25.4 mm

Figure 23. Graph. Maximum average tensile stress in concrete versus time (L = 1.524 m (60 inches)) and different GFRP reinforcing ratios, ρ).

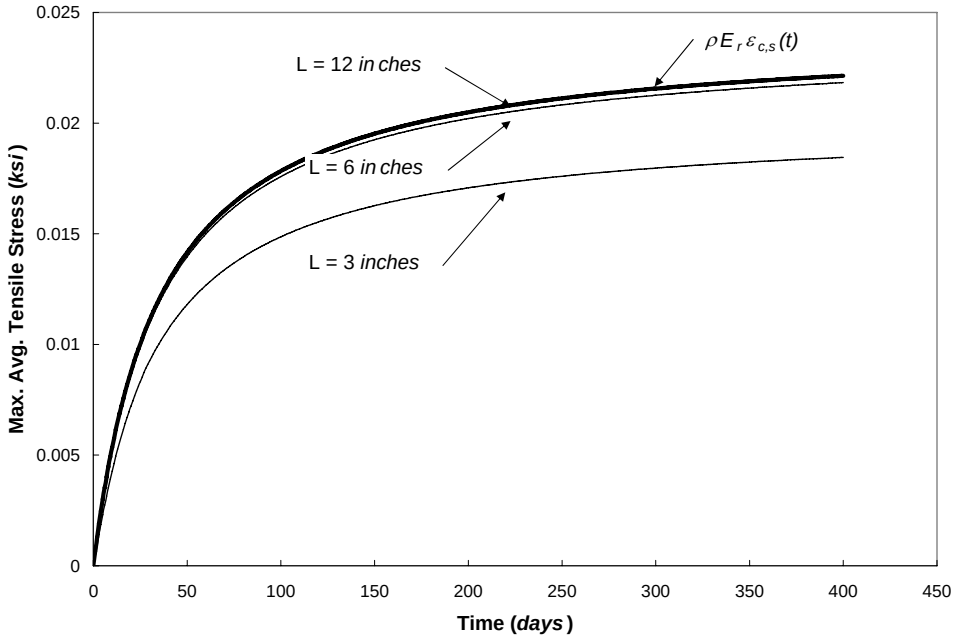

1 ksi = 6.89 MPa: 1 inch = 25.4 mm

Figure 24. Graph. Maximum average tensile stress in concrete versus time (ρ = 0.00519 GFRP and different slab lengths, L).

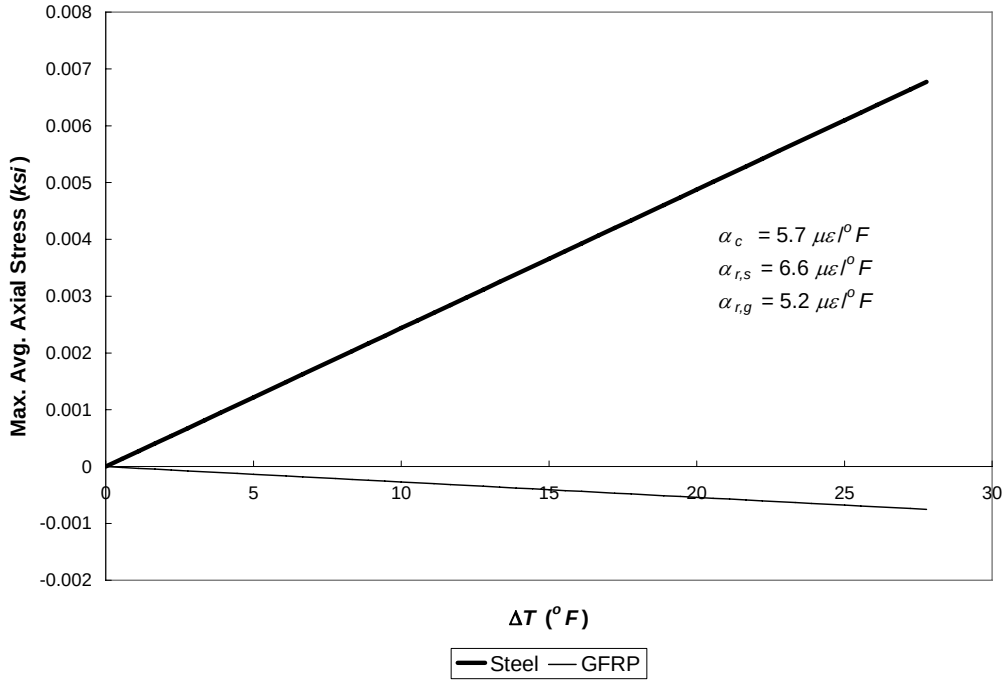

1 (ΔT °F) = 0.56 (ΔT °C); 1 ksi = 6.89 MPa; 1 με/°F = 1.80 με/°C

Figure 25. Graph. Maximum average axial stress in concrete versus temperature change (ρ = 0.00519 and L = 1.524 m (60 inches)).

The siliceous river gravel aggregate concrete has a CTE higher than both CTEs of steel and GFRP rebars, and temperature increases lead to compressive stress development in the concrete for both reinforcement cases, as shown in figure 26. These compressive and tensile states are reversed as temperature decreases (negative ΔT). As can be seen in both figures 25 and 26, the absolute values of thermal concrete stresses from GFRP rebar are less than those from steel rebar, mainly because of GFRP rebar's lower elastic modulus. In addition, both the magnitude and sign of the stress caused by temperature variation can be controlled by using different combinations of concrete and reinforcement CTEs.

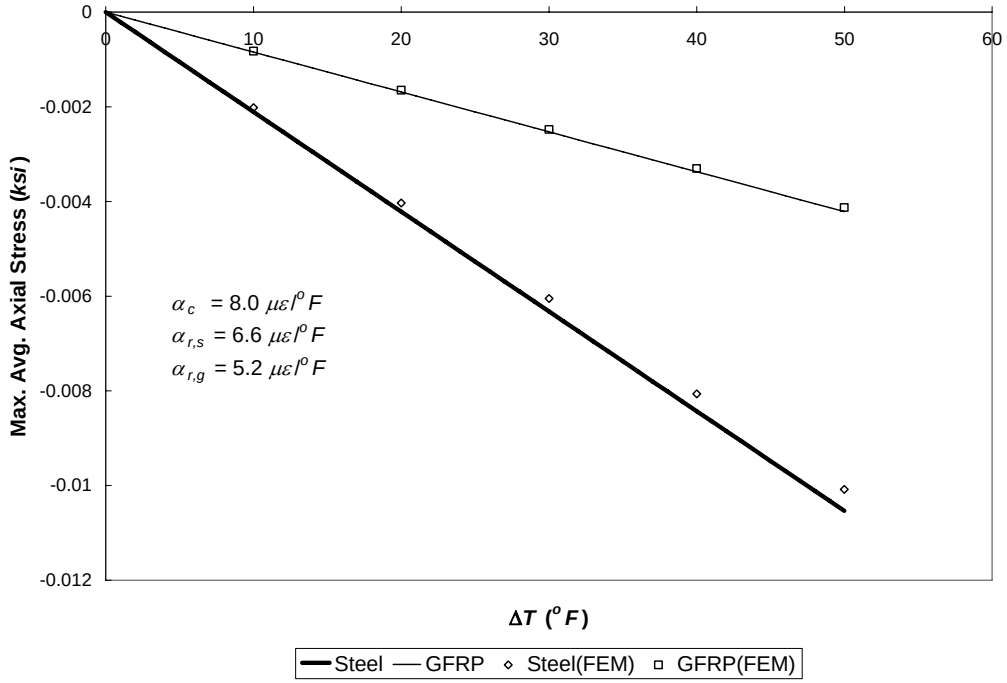

1 (ΔT ^{o}F) = 0.56 (ΔT ^{o}C); 1 ksi = 6.89 MPa; 1 με/^{o}F = 1.80 με/^{o}C

Figure 26. Graph. Maximum average axial stress in concrete versus temperature change (ρ = 0.00519 and *L* = 1.524 m (60 inches)).

COMPARISON WITH FINITE ELEMENT MODEL

Using the FE analysis program, ABAQUS, a finite element model (FEM) of a freely supported, reinforced concrete slab has been created, and the results from the shrinkage and thermal analytical models are compared with the FEM results. The concrete slab is modeled as four-node, 2-D elements under plane stress conditions, and the reinforcement is modeled as beam elements with circular cross sections. The thickness of the concrete 2-D plane stress elements is the width, *B*, of the concrete prismatic model. The bond-slip between concrete and reinforcement is modeled by using horizontal spring elements, and the bond is assumed to be perfect. All of the material properties are assumed to be the same as those used in the analytical model (table 1); in this study, the spring stiffnesses used to simulate the perfect bond, which depend on Young's modulus of concrete, are 1.303 GN/m (7,443 kip/inch) and 1.251 GN/m (7,145 kip/inch) for granite concrete and siliceous river gravel concrete, respectively. The comparison (figures 20 and 24) between the analytical and FE methods shows a good agreement of the maximum average axial stresses in the concrete.

The axial concrete stress distribution along the longitudinal (*x*-) direction for a GFRP-reinforced slab with a temperature variation of –27.8 ^{o}C (–50 ^{o}F) has also been calculated using both analytical and FE methods (figure 27).

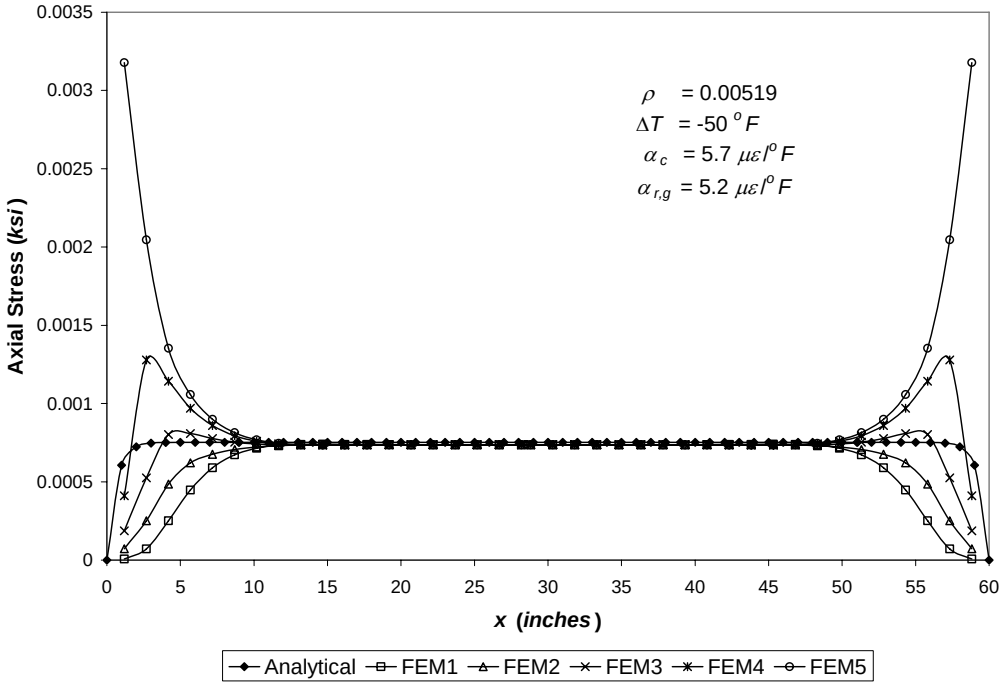

1 inch = 25.4 mm; 1 ksi = 6.89 MPa; 1 (ΔT °F) = 0.56 (ΔT °C); 1 με/°F = 1.80 με/°C

Figure 27. Graph. Axial stress in concrete versus longitudinal location (comparison between analytical and FEM results).

Figure 27 shows the concrete stresses located at five different longitudinal layers of concrete. The layers are laterally located from the concrete surface to the interface between the concrete and reinforcement, and are represented by using the nomenclature of FEM1 through FEM5 in the figure; FEM1 represents the surface layer, and FEM5 represents the layer closest to the reinforcement. The results show that the axial stresses from the analytical model, which are averaged in the radial (*r*-) direction, agree well with the axial stresses from all the layers of the concrete FE element as the *x*-location approaches the middle of the section. From the FE results, it can be seen that the axial stresses are varied through the depth around the ends of the slab. This is simply caused by the fact that, along the depth direction, the more drastic change in axial displacement occurs around the ends rather than around the middle section due to the restraint from the reinforcement. The comparison also shows that the analytical solution of average axial concrete stresses (figure 18) is valid throughout the longitudinal (*x*-) direction, especially in the vicinity of the slab's middle section, proving the validity of the maximum average axial stresses in concrete at $x = L/2$ as previously shown.

CHAPTER 4. EXPERIMENTAL STUDY

ANALYTICAL SOLUTIONS EXPERIMENTALLY APPLICABLE TO FREELY SUPPORTED REINFORCED CONCRETE SLAB

In this study, a test to assess the validity of the analytical model was conducted. Since the experimental mechanical behavior of the reinforced concrete slab under concrete volume change can be estimated in terms of strain, the strain equation needs to be derived from the analytical model. The strain, $(\varepsilon_c)_{gage}$, that can be measured by the strain gage on the reinforced concrete slab is the resulting concrete strain due to the concrete volume change, ε_c, and the restraint from reinforcement, $(\varepsilon_c)_{avg}$.

$$(\varepsilon_c)_{gage} = \varepsilon_c + (\varepsilon_c)_{avg}$$

Figure 28. Equation. $(\varepsilon_c)_{gage}$.

where $(\varepsilon_c)_{avg} = (\sigma_c)_{avg}/E_c$. Thus,

$$(\varepsilon_{c,s})_{gage} = -\frac{t}{35+t}(\varepsilon_{c,s})_{ult}\left\{1-\rho\frac{E_r}{E_c(t)}\left[1-\frac{\cosh\beta\left(\frac{L}{2}-x\right)}{\cosh\beta\frac{L}{2}}\right]\right\}$$

Figure 29. Equation. $(\varepsilon_{c,s})_{gage}$.

and

$$(\varepsilon_{c,t})_{gage} = \Delta T\left\{\alpha_c-\rho\frac{E_r}{E_c}(\alpha_c-\alpha_r)\left[1-\frac{\cosh\beta\left(\frac{L}{2}-x\right)}{\cosh\beta\frac{L}{2}}\right]\right\}$$

Figure 30. Equation. $(\varepsilon_{c,t})_{gage}$.

where $(\varepsilon_{c,s})_{gage}$ and $(\varepsilon_{c,t})_{gage}$ are the strains due to concrete shrinkage and temperature variation, respectively. The $(\varepsilon_c)_{avg}$ in figure 28 is obtained from $(\sigma_c)_{avg}$ that is analytically derived for the averaged concrete stresses in the radial (r-) direction at any x-locations. Based on the previous discussion of FE model agreement (figure 27), this value can still adequately represent the reinforcement restraint-induced strain which is uniformly distributed throughout the lateral direction at around the longitudinal middle of the slab. The experiment was conducted considering the temperature variation-induced strain on

three laboratory slab specimens: a plain concrete slab, a steel (number 4 rebar with a radius of 6.35 mm (0.25 inch); $\rho = 0.01695$) reinforced concrete slab, and a GFRP (number 4 rebar) reinforced concrete slab.

CTE MEASUREMENT OF REINFORCEMENTS

The mechanical behavioral differences between the aforementioned slabs under a temperature change can be presented in terms of the differences in the deformations developed in the slabs. In order for the analytical model to predict the strain differences between the slabs under the temperature change, the CTEs of the reinforcements used in the slabs should be known. Therefore, an experiment to measure the CTEs of the steel and GFRP rebars using strain gages was conducted prior to the experiment on the slabs. The experimental method using strain gages has been standardized as an alternative method to accurately measure the CTEs of a test material with respect to that of any reference material having a known CTE.[31,32] Rebars—15.24 cm (6 inch) long number 4 steel and GFRP—were prepared along with a reference material, titanium silicate, having an extremely low CTE (about 0.0 με/°F) over the temperature range of interest (from –29 °C (–0.2 °F) to 49 °C (120.2 °F)); grade 60 deformed steel rebar and the GFRP rebar manufactured by Marshall Industry Composite, Inc., were employed. A strain gage (EA-06-125BB-120; Measurement Group, Inc.) was attached at the middle of each of the steel and GFRP rebars in the longitudinal direction as well as at that of the titanium silicate strip, as shown in figures 31, 32, and 33.

Figure 31. Photo. Number 4 steel rebar specimen for CTE measurement.

Figure 32. Photo. Number 4 GFRP rebar specimen for CTE measurement.

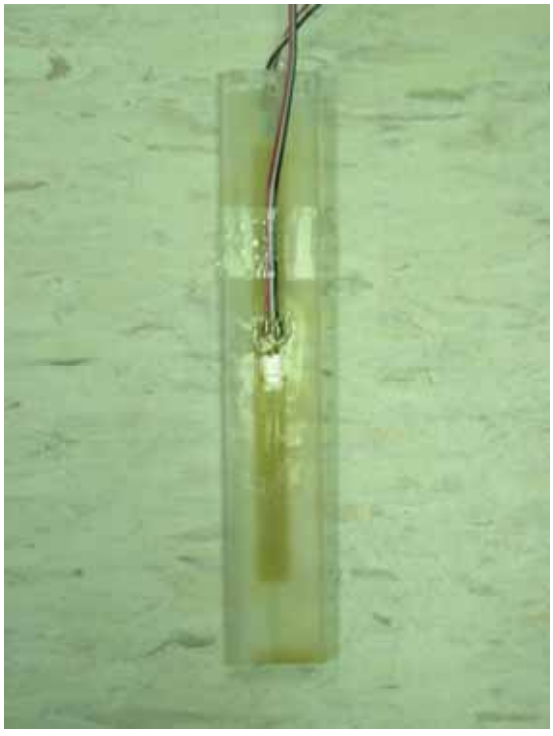

Figure 33. Photo. Titanium silicate strip specimen for CTE measurement.

The steel and GFRP rebars were then housed in the environmental chamber along with the titanium silicate strip so that both rebars and the titanium silicate strip were subjected to the cyclic temperature change simultaneously. The rebars and titanium silicate strip were suspended from one end so that friction could not impede their expansion or contraction due to temperature change. The measurement was conducted three times for each of the steel and GFRP reinforcing rebars. Two cycles of temperature change were applied for each measurement. Each cycle of temperature change consisted of 43 °C (109.4 °F) → 49 °C (120.2 °F) → 22 °C (71.6 °F) → –29 °C (–20.2 °F) → 43 °C (109.4 °F), would take about 5 d.

The output of the strain gage induced by temperature change is defined as thermal output. The thermal output of the gage is caused by combined resistance changes resulting from (1) changes with temperature in the resistivity of the gage grid alloy, and (2) the mechanical strain of the strain grid by an amount equal to the difference in the expansion coefficient between the gage grid alloy and the test material. The thermal output does not directly represent genuine strain of the test material induced by the temperature change and must be adjusted accordingly. As given in figure 34, the strain of the test material can be obtained by rearranging the equation

$$\alpha_{T/M} - \alpha_{R/M} = \frac{(\varepsilon_{T/O})_{T/M} - (\varepsilon_{T/O})_{R/M}}{\Delta T}$$

Figure 34. Equation. $\alpha_{T/M} - \alpha_{R/M}$.

where $\alpha_{T/M}$ and $\alpha_{R/M}$ = CTEs of test and reference materials, respectively; and $(\varepsilon_{T/O})_{T/M}$ and $(\varepsilon_{T/O})_{R/M}$ = thermal outputs of test and reference materials, respectively. Since the CTE of the reference material (titanium silicate) is 0.0 $\mu\varepsilon/^{o}F$ in this study, figure 34 becomes

$$\alpha_{T/M}\,\Delta T = (\varepsilon_{T/O})_{T/M} - (\varepsilon_{T/O})_{R/M}.$$

Figure 35. Equation. $\alpha_{T/M}\,\Delta T$.

The difference between the thermal outputs of the test and reference materials, which are obtained experimentally, can then represent the strain of the test material induced by the temperature change. The CTE of the test material can thus be obtained since ΔT is experimentally known. For each measurement, the thermal output was set to 0 με at a reference temperature, T_o, of about 43° C (109.4 °F). From each rebar as well as from titanium silicate strip, the thermal output was collected at each temperature level, and the CTE of each rebar was obtained. It was also observed from the measurements that the thermal outputs were highly repeatable at a similar measured temperature, and the CTE of each rebar was fairly consistent at different applied temperature levels as shown in table 2 and figure 36, which correlate to the third measurement. The average CTEs from the three measurements were about 11.88 με/°C (6.6 με/°F) for steel rebar and 9.18 με/°C (5.1 με/°F) for the GFRP rebar.

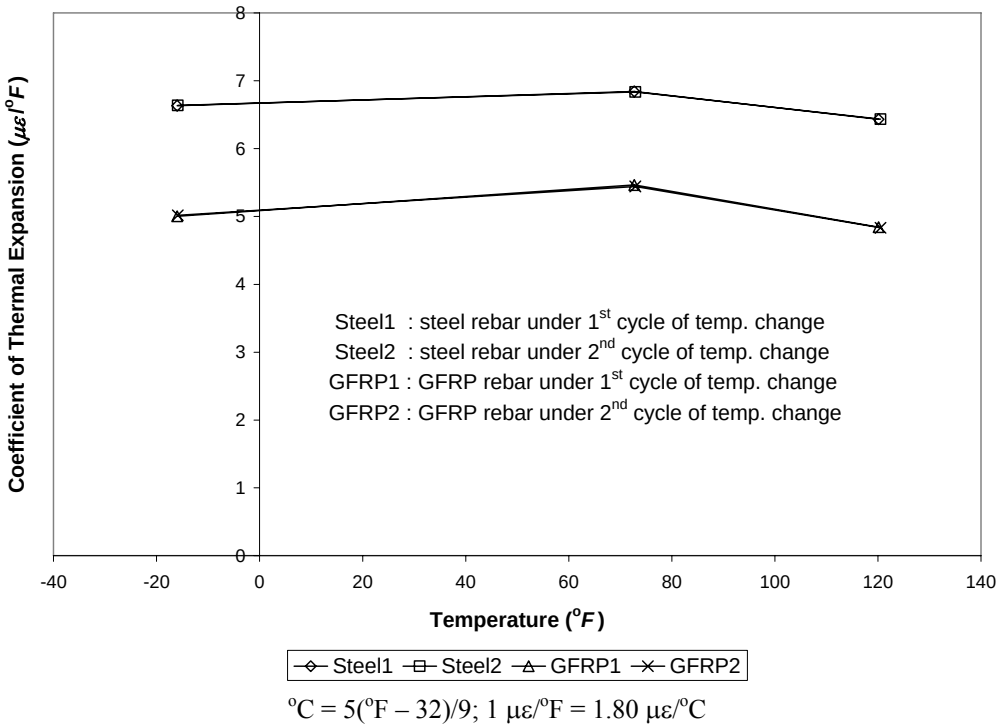

°C = 5(°F – 32)/9; 1 με/°F = 1.80 με/°C

Figure 36. Graph. Coefficient of thermal expansion versus temperature for reinforcing rebars from third measurement.

EXPERIMENT ON FREELY SUPPORTED REINFORCED CONCRETE SLAB SUBJECTED TO TEMPERATURE VARIATION

The three laboratory slab specimens were cast and cured for about 5 months at room temperature and 40~45 percent RH before the experiment. Drying shrinkage effect would be negligible during the experiment. A thermocouple was set in the center of each slab before the concrete cast, and a strain gage (N2A-06-40CBY-120; Measurement Group, Inc.) was attached in the center of the upper surface of each slab after the curing process. The slabs were then subjected to cyclic temperature changes in an environmental chamber with temperature and humidity control. The schematic details of the specimens are shown in figure 37, and photos are shown in figures 38 and 39.

Table 2. Thermal outputs and CTEs of steel and GFRP rebars at different temperature levels (from third measurement).

Temperature (T; ^{o}F[1])	Elapsed time (h)	Thermal Output ($\varepsilon_{T/O}$; με)			$\Delta T^2 = T - T_o$[3] (^{o}F)	$(\varepsilon_{T/O})_{T/M} - (\varepsilon_{T/O})_{R/M}$ (με)		$\alpha_{T/M}$ (με/^{o}F[4])	
		Titanium silicate	Steel	GFRP		Steel	GFRP	Steel	GFRP
109.2	0	0	0	0	~	~	~	~	~
120.1	24	–74	–3	–21	10.9	70	53	6.4	4.8
72.7	48	247	–3	47	–36.5	–250	–199	6.8	5.5
–16.0	60	633	–198	6	–125.2	–831	–627	6.6	5.0
110.2	87	2	0	–1	~	~	~	~	~
109.7	94	1	0	–1	~	~	~	~	~
120.5	144	-76	–4	–22	11.3	73	55	6.4	4.8
72.9	168	246	–2	48	–36.3	–248	–198	6.8	5.4
–15.9	180	631	–199	3	–125.1	–830	–628	6.6	5.0
110.0	207	1	0	1	~	~	~	~	~
							Average:	6.6	5.1

[1] ^{o}C = 5(^{o}F – 32)/9.
[2] 1 (ΔT ^{o}F) = 0.56 (ΔT ^{o}C);
[3] T_o = 42.9 ^{o}C (109.2 ^{o}F).
[4] 1 με/^{o}F = 1.80 με/^{o}C

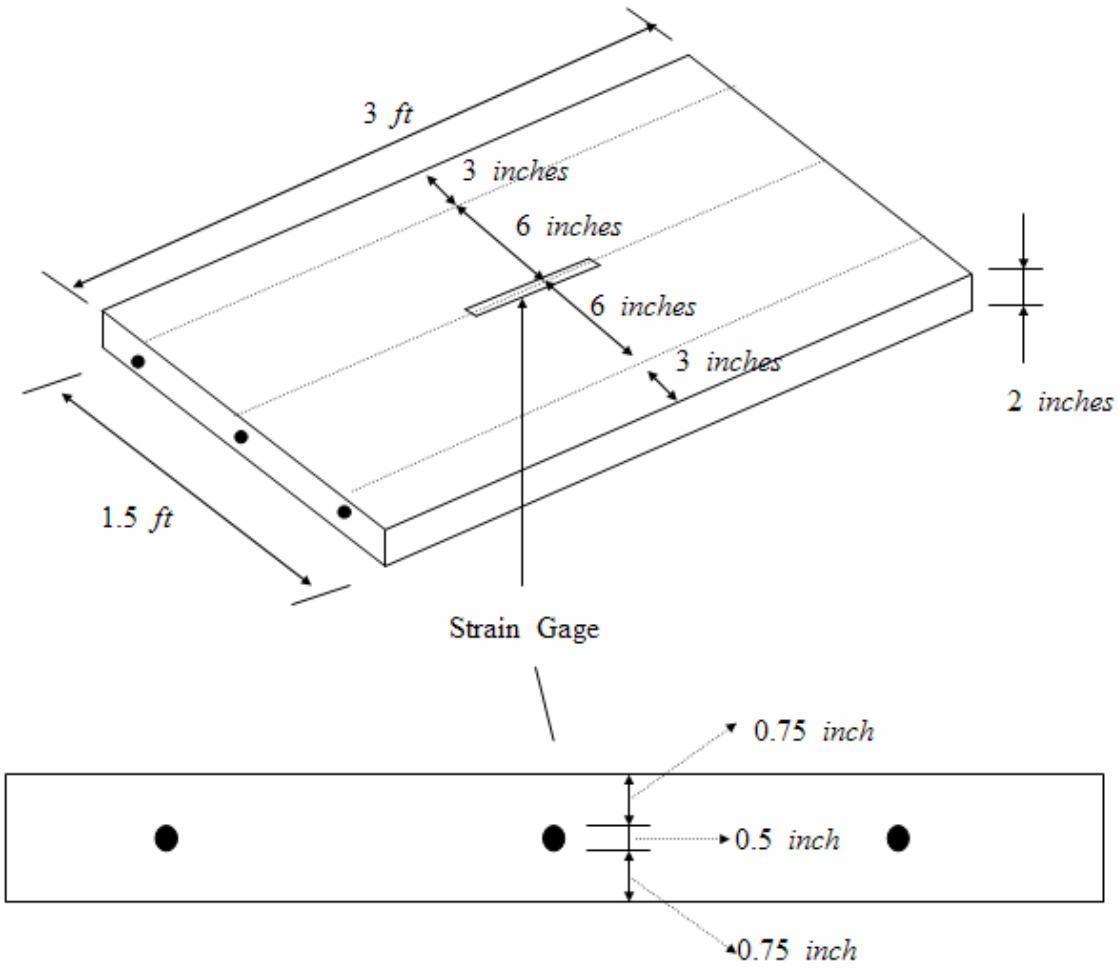

1 inch = 25.4 mm; 1 ft = 0.305 m

Figure 37. Drawing. Schematic details of concrete slabs used in experiment.

Figure 38. Photo. Concrete slab molds before concrete cast.

Figure 39. Photo. Concrete slabs attached with strain gages.

In the concrete slab experiment, each slab was supported on three lubricated rollers in order to minimize the frictional effect. The experiment was also conducted three times, and, at each time, the slabs were subjected to two cycles of temperature change as the CTE measurement experiment was. The titanium silicate strip, now attached with a strain gage (N2A-06-40CBY-120) at its middle in a longitudinal direction, was also employed in the experiment on the slabs. The experiment followed the same procedure as previously mentioned. A concrete CTE of 9.36 με/°C (5.2 με/°F), which was an average of the CTEs measured from the plain concrete slab, was utilized for the analytical calculation using figure 31, and the results are shown in figure 40. In addition, the Young's modulus of concrete of 30.5 GPa (4,420 ksi) used in the calculation was obtained experimentally from the results of the compressive tests of three 15.24- by 0.48-cm (6- by 12-inch) concrete cylinders cast at the same time as the concrete slabs. In the figure, it is predicted that the axial concrete strains calculated for the steel-reinforced slab have higher contraction magnitudes (shown as negative values) than those for the plain and GFRP-reinforced slabs under temperature drop. This is reasonable since the CTE of the steel rebar is higher than those of the concrete and GFRP so that the steel reinforcement adds more contraction on the concrete. Since the GFRP rebar used has a CTE similar to that of the concrete, the strain values calculated for the GFRP-reinforced slab are also close to those for the plain slab.

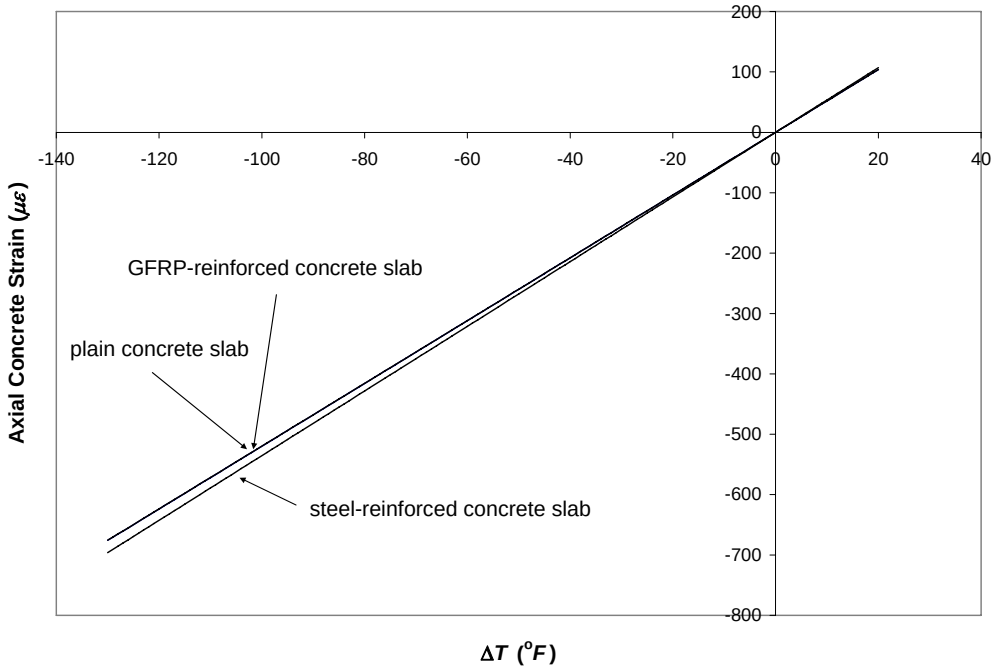

1 (ΔT °F) = 0.56 (ΔT °C)

Figure 40. Graph. Axial concrete strain at midspan versus temperature change from analytical calculation.

In figures 41, 42, and 43, the axial concrete strains measured at the midspan of each slab over the temperature changes ranging from T = +49 °C (+120.2 °F) to –29 °C (–20.2 °F) are compared with the analytical calculations which employ the aforementioned material properties; some other material properties necessary for the analysis—such as the Poisson ratio of the concrete and the Young moduli of the steel and GFRP rebars—are the same as those listed in table 1. In the figure, the nomenclature of Test#*X*-*Y* represents the test results from the *Y*th temperature change cycle of *X*th test. It is shown in the comparison that the experimentally obtained strains are fairly well distributed around the calculated strains, which are shown as solid lines. In addition, the measured strains under freezing temperatures seem to have contraction magnitudes that are somewhat smaller than the calculated values. This may result from the expansion of concrete and the higher Young's modulus of concrete caused by moisture freezing in the concrete. The experimentally measured strains are tabulated in table 3.

Similar results are also expected as the concrete shrinkage is considered. Therefore, the analytical model can be a useful means of evaluating the stress or strain level around the middle of a freely supported reinforced slab that is subjected to concrete shrinkage and temperature change.

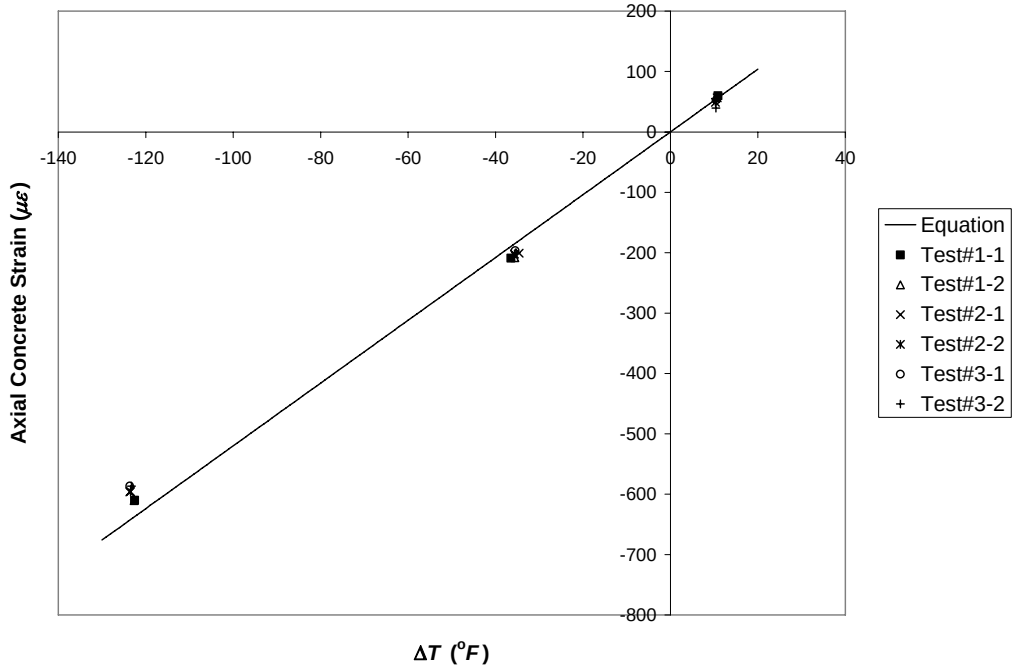

1 (ΔT °F) = 0.56 (ΔT °C)

Figure 41. Graph. Axial concrete strain at midspan versus temperature change for plain concrete slab (reference temperature, T_o = about 42.39 °C (108.3 °F)).

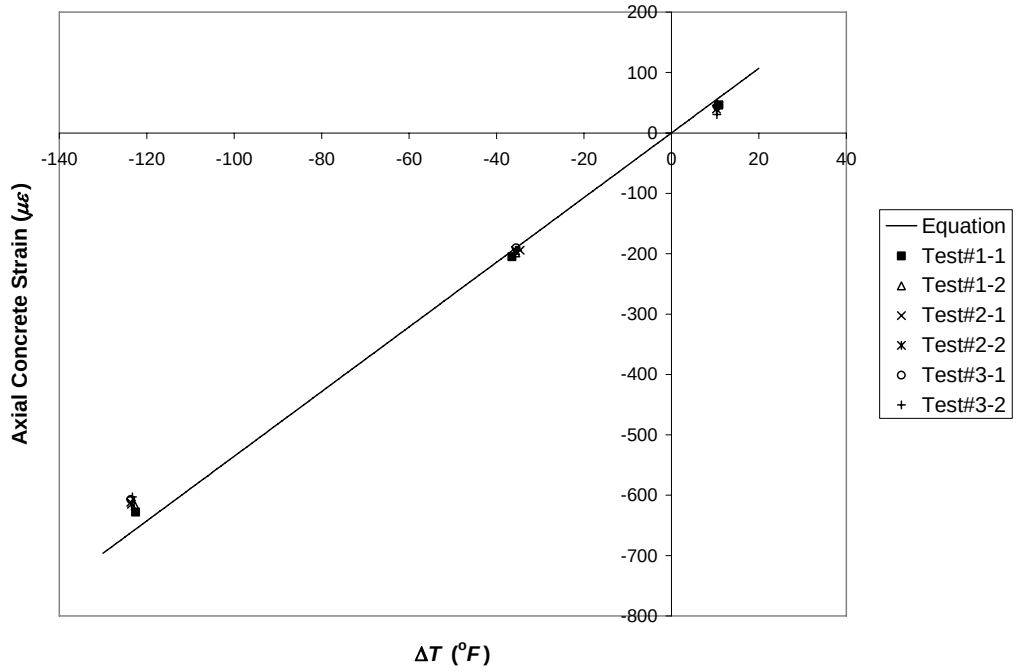

1 (ΔT °F) = 0.56 (ΔT °C)

Figure 42. Graph. Axial concrete strain at midspan versus temperature change for steel-reinforced concrete slab (reference temperature, T_o = about 42.39 °C (108.3 °F)).

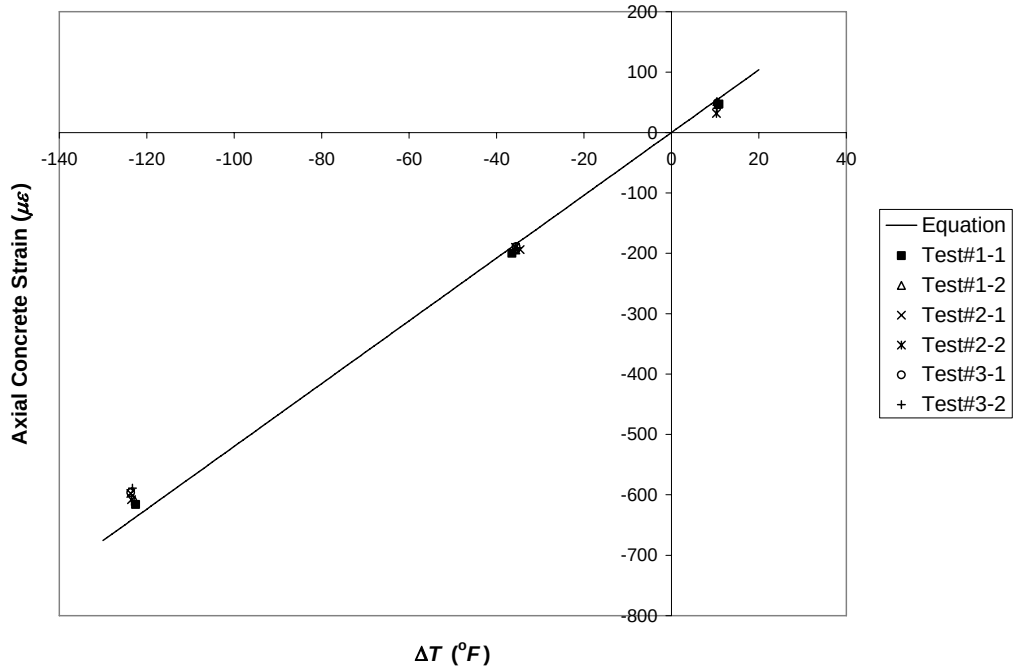

1 (ΔT °F) = 0.56 (ΔT °C)

Figure 43. Graph. Axial concrete strain at midspan versus temperature change for GFRP-reinforced concrete slab (reference temperature, T_o = about 42.39 °C (108.3 °F)).

Table 3. Thermal outputs of slabs at different temperature levels (TS: titanium silicate; PS: plain slab; S-RS: steel-reinforced slab; G-RS: GFRP-reinforced slab).

		Temperature (T; °F[1])	Elapsed Time (h)	Thermal Output ($\varepsilon_{T/O}$; $\mu\varepsilon$)				$\Delta T^2 = T - T_o$ (°F)	$(\varepsilon_{T/O})_{T/M} - (\varepsilon_{T/O})_{R/M}$ ($\mu\varepsilon$)		
				TS	PS	S-RS	G-RS		PS	S-RS	G-RS
1st Test: T_o = 108.0°F	1st Cycle	108.0	0	0	0	0	0	~	~	~	~
		118.9	24	–68	–8	–22	–21	10.9	60	46	47
		71.5	48	224	15	19	25	–36.5	–209	–205	–200
		–14.6	60	564	–46	–64	–52	–122.6	–610	–628	–616
		107.0	87	2	10	16	10	~	~	~	~
	2nd Cycle	108.0	94	3	5	11	8	~	~	~	~
		118.4	144	–70	–13	–21	–18	10.4	57	49	51
		72.4	168	223	15	24	28	–35.6	–208	–199	–195
		–14.7	180	563	–47	–55	–47	–122.7	–610	–618	–611
		108.1	207	3	7	13	12	~	~	~	~
2nd Test: T_o = 108.3°F	1st Cycle	108.3	0	0	0	0	0	~	~	~	~
		119.0	24	–69	–13	–23	–22	10.7	57	46	47
		73.7	48	223	22	29	29	–34.6	–201	–194	–194
		–15.4	60	562	–34	–50	–36	–123.7	–596	–612	–598
		108.6	87	2	4	5	–5	~	~	~	~
	2nd Cycle	108.7	94	0	–7	–6	–14	~	~	~	~
		118.6	144	–73	–24	–33	–41	10.3	49	40	32
		72.6	168	218	15	23	28	–35.7	–202	–195	–190
		–15.2	180	559	–36	–56	–49	–123.5	–596	–615	–608
		108.5	207	–1	1	2	–3	~	~	~	~

[1] °C = 5(°F – 32)/9.

[2] 1 (ΔT °F) = 0.56 (ΔT °C)

Table 3. Thermal outputs of slabs at different temperature levels
(TS: titanium silicate; PS: plain slab; S-RS: steel-reinforced slab; G-RS: GFRP-reinforced slab)
Continued

		Temperature (T; ^{o}F)	Elapsed Time (h)	Thermal Output ($\varepsilon_{T/O}$; $\mu\varepsilon$)				$\Delta T=T-T_o$ (^{o}F)	$(\varepsilon_{T/O})_{T/M}-(\varepsilon_{T/O})_{R/M}$ ($\mu\varepsilon$)		
				TS	PS	S-RS	G-RS		PS	S-RS	G-RS
3rd Test: $T_o = 108.5\ ^{o}F$	1st Cycle	108.5	0	0	0	0	0	~	~	~	~
		119.0	24	–68	–15	–24	–19	10.5	53	44	49
		73.0	48	222	25	31	33	–35.5	–197	–190	–189
		–15.2	60	560	–27	–47	–37	–123.7	–587	–607	–596
		109.0	87	0	–4	-6	-5	~	~	~	~
	2nd Cycle	108.7	94	–1	–12	–15	–10	~	~	~	~
		118.9	144	–70	–31	–40	–30	10.4	39	31	40
		73.2	168	220	20	25	28	–35.3	–200	–195	–191
		–14.8	180	557	–30	–46	–32	–123.3	–587	–603	–589
		109.0	207	1	–7	-9	-6	~	~	~	~

CHAPTER 5. FE STUDY OF DESIGN CONSIDERATIONS FOR CRCP

FE ANALYSIS OF A 1.524-M (5-FT) CRCP SEGMENT

As can be seen in figures 22 through 26, the tensile stress levels in concrete caused by both concrete shrinkage and temperature variation are far below the tensile strength of normal concrete for the free slab. Other restraining forces acting on a given concrete slab, such as friction from the subbase under concrete pavements or restraints from reinforcement ties to neighboring slabs, need to be considered. When these restraints are considered, the overall resulting tensile stress level in the concrete will increase, possibly exceeding the concrete tensile strength and causing cracks in the concrete slab.

The CRCPs considered in the FE analyses have been assumed to have transverse cracks equally spaced at 1.524 m (5 ft (60 inches)) and were subjected to the concrete shrinkage and temperature variation. Since the cracks in the CRCP are assumed to be spaced equally, the longitudinal reinforcement at the crack is constrained in both longitudinal and rotational directions. Therefore, only a representative slab segment was needed to model the CRCP. The length of the slab segment, L, is equal to the crack spacing. While longitudinal reinforcement of number 6 rebars with a radius (r) of 9.53 mm (0.375 inch) was considered in the FEM analysis, the influence of transverse reinforcement was ignored. The bond-slip behaviors between the concrete and reinforcement and between the concrete slab and subbase were modeled by using horizontal spring elements. The underlying layers are modeled as an elastic foundation with an elastic spring constant of 108.583 megapascals per meter (MPa/m) (400 poundsforce per square inch per inch ($lbf/in^2/inch$)). The FE model of the CRCP slab segment has been assumed to be subjected to a concrete shrinkage at 28 d of 355.6 με and a temperature change (ΔT) of –27.8 °C (–50 °F) and –16.7 °C (–30 °F) at the top and bottom of the slab segment, respectively. The temperature varies linearly from the top to the bottom. All of the other model parameters and material properties used are listed in table 4, and the schematic details of the FE model are depicted in figure 44; the properties of GFRP rebar are assumed in this analysis.

Table 4. Model parameters and material properties used in FE study.

Parameter and Properties	Value
Width, B (cm (inches))	15.24 (6)
Height, H (cm (inches))	25.40 (10)
Young's modulus of concrete at 28 d, $E_{c,28}$ (GPa (× 10^6 lbf/in^2))	33.10 (4.80)[1] and 34.48 (5.00)[2]
Poisson's ratio of concrete, ν_c	0.20
Young's modulus of steel rebar (GPa (× 10^6 lbf/in^2))	200.00 (29.00)
Longitudinal Young's modulus of GFRP rebar (GPa (× 10^6 lbf/in^2))	40.80 (5.92)
CTE of concrete, α_c (με/°C (με/°F))	10.26 (5.7)[1] and 14.40 (8.0)[2]
CTE of steel rebar, $\alpha_{r,s}$ (με/°C (με/°F))	11.88 (6.6)
CTE of GFRP rebar, $\alpha_{r,g}$ (με/°C (με/°F))	9.07 (5.04)

[1]Granite coarse aggregate used.
[2]Siliceous river gravel coarse aggregate used.
1 megapoundforce per square inch (10^6 lbf/in^2) = 6.89 gigapascal (GPa)

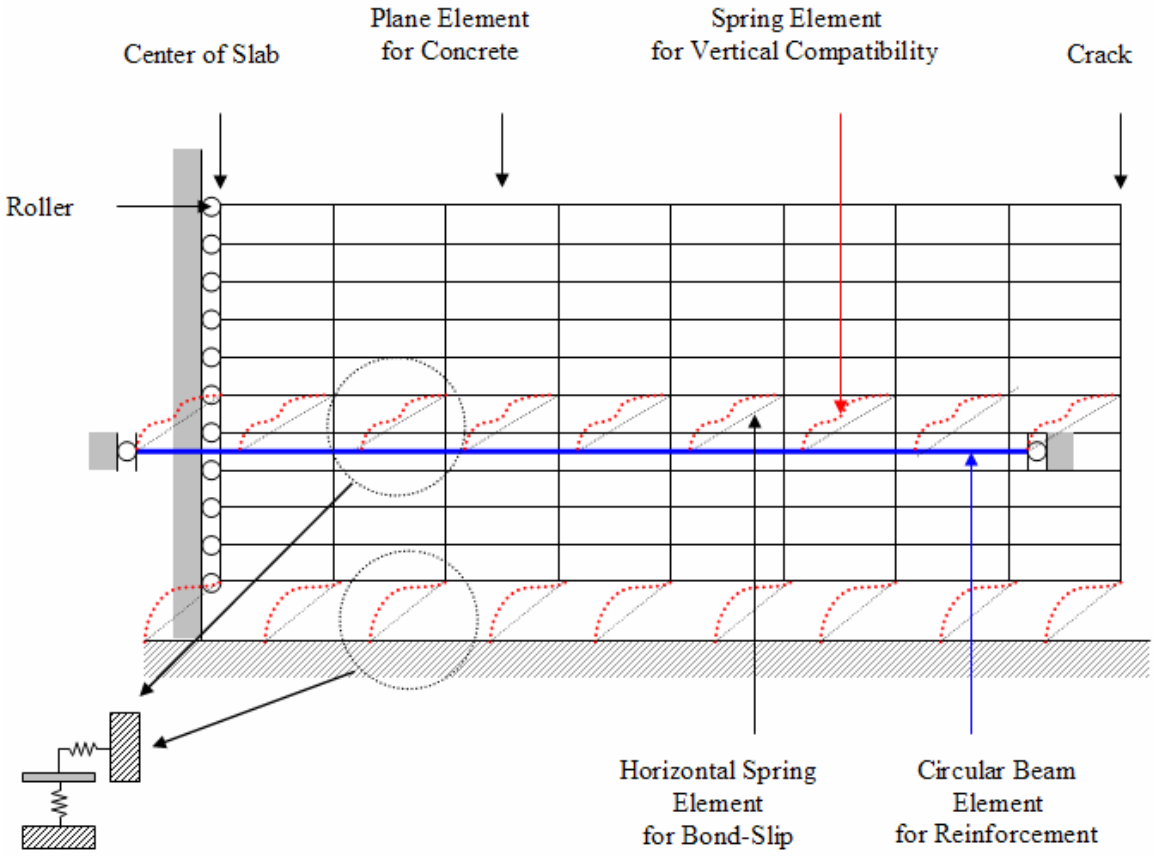

Figure 44. Drawing. Schematic details of a 2-D CRCP finite element model.

In the FE analysis, the CRCP design parameters—such as the CTE of concrete, the friction from the pavement's subbase, and the bond-slip between concrete and reinforcement—were studied to assist in understanding their effects on stress development and crack width in the CRCP.

Effect of Concrete CTE on Stress Development in CRCP

Two different types of concrete, with granite aggregate or siliceous river gravel aggregate, have been adopted in the stress analysis of the CRCP slab segment. The CTEs of granite and siliceous river gravel concrete are 10.26 με/°C (5.7 με/°F) and 14.40 με/°C (8.0 με/°F), respectively.[30] In addition, the steel-reinforced CRCP slab segment is analyzed for comparison with the GFRP-reinforced one. The bond between the concrete and reinforcement is assumed to be perfect, and the bond-slip between the concrete slab and subbase was represented using a spring stiffness of 236.409 kilonewton per meter (kN/m) (1,350 poundsforce per inch (lbf/inch)), which is simulated for a flexible subbase or a lime-treated clay subbase, having the bond-slip stiffness per unit area of 40.719 MPa/m (150 lbf/in^2/inch) with respect to the concrete slab. The spring stiffness corresponds to a concrete element with a horizontal length of 3.81 cm (1.5 inches) and a thickness in the *z*-direction of 15.24 cm (6 inches).

Figures 45 and 46 show the FE results of axial tensile stresses developed on the concrete surface along the longitudinal (*x*-) direction, considering the aforementioned restraining conditions. The maximum tensile stress level for the GFRP-reinforced slab segment at the *x*-midpoint, shown in figure 42, is much higher compared with those for the freely supported reinforced concrete slab, shown in figures 22 through 26. As expected, considering those restraints in the CRCP model increases the tensile stress level in concrete. As can be seen in both figures 45 and 46, because of the low Young's modulus in the GFRP rebar, the tensile stresses for the GFRP-reinforced concrete are always smaller than those for the steel ones. The use of GFRP rebar as the reinforcement might lead to larger crack spacings followed by wider crack widths in the CRCP. If it is necessary to shorten the crack spacing or narrow the crack width, it can be achieved by using a larger amount of reinforcement or by adjusting the concrete properties, the subbase restraints, or bonding between the concrete and reinforcement. For reference, AASHTO guidelines indicate that the crack spacing should be no more than 2.438 m (8 ft) to minimize the incidence of crack spalling and no less than 1.067 m (3.5 ft) to minimize the potential for the development of punchouts, and the allowable crack width should not exceed 1 mm (0.04 inch) for the steel-reinforced CRCP.[2]

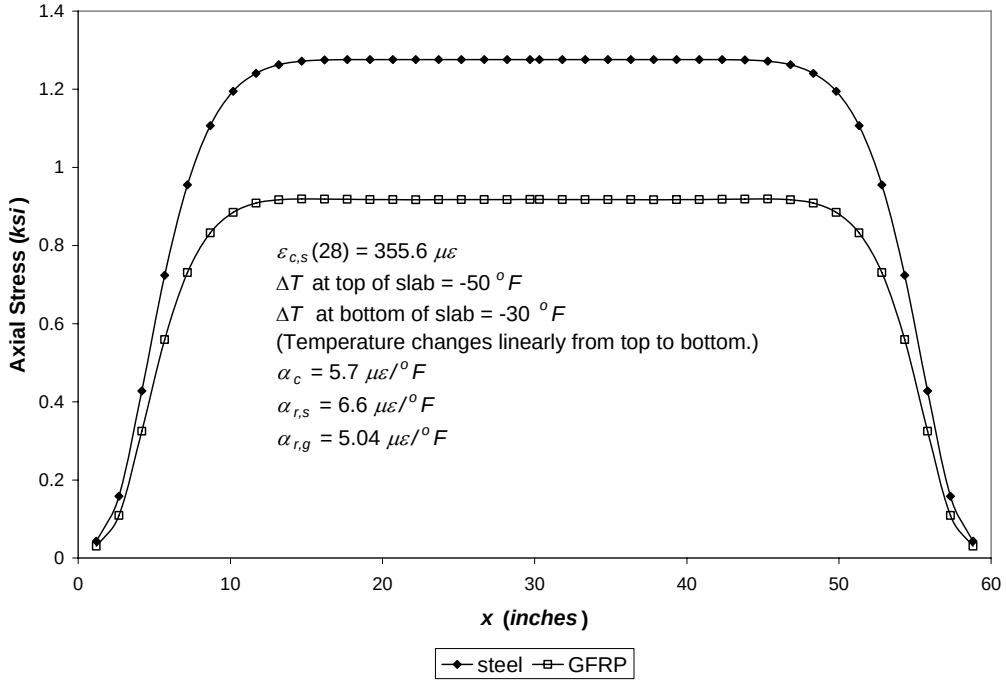

1 inch = 25.4 mm; 1 ksi = 6.89 MPa; 1 (ΔT °F) = 0.56 (ΔT °C); 1 με/°F = 1.80 με/°C

Figure 45. Graph. Axial tensile stress on concrete surface versus longitudinal location of a 1.524-m (5-ft) CRCP segment with ρ = 0.00739 and α_c = 10.26 με/°C (5.7 με/°F).

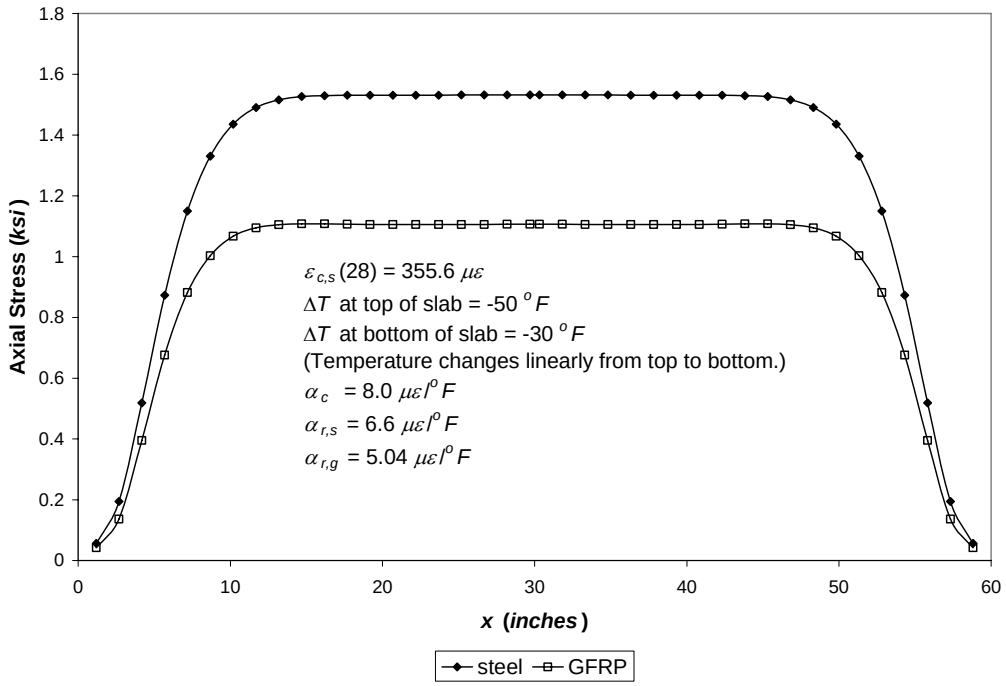

1 inch = 25.4 mm; 1 ksi = 6.89 MPa1 (ΔT °F) = 0.56 (ΔT °C);1 με/°F = 1.80 με/°C

Figure 46. Graph. Axial tensile stress on concrete surface versus longitudinal location of a 1.524-m (5-ft) CRCP segment with ρ = 0.00739 and α_c = 14.40 με/°C (8.0 με/°F).

It can be seen in the comparison between figures 45 and 46 that the tensile stress level in concrete for the granite concrete with a CTE of 10.26 με/°C (5.7 με/°F) is lower than that for the siliceous river gravel concrete with a CTE of 14.40 με/°C (8.0 με/°F). This is because the difference between CTEs of concrete and reinforcement for the granite concrete is smaller than that for the siliceous river gravel concrete. Therefore, the tensile stress in concrete can be reduced by using concrete with lower CTE. Regardless of the concrete CTEs, the maximum tensile stresses in concrete for both steel- and GFRP-reinforced slab segments are much higher than the concrete tensile strength, and all the slab segments will presumably be cracked at their midspan due to the given temperature variation and shrinkage conditions. The concrete tensile strengths for the granite and siliceous river gravel concretes are about 2.90 MPa (420 lbf/in^2) and 2.55 MPa (370 lbf/in^2), respectively, with a concrete compressive strength, f_c', of about 27.58 MPa (4,000 lbf/in^2).

The axial stress distributions in the reinforcements along the longitudinal (*x*-) direction for two different concrete CTEs are shown in figures 47 and 48. While the reinforcements around the middle are under low compression, those around the crack (the ends of the slab segment) are under high tension. Because of the stiffness compatibility between GFRP and concrete, the tensile stresses in the GFRP reinforcements are lower than those in the steel reinforcements. The tensile reinforcement stress for the lower concrete CTE (figure 49) is also lower than that for the higher concrete CTE (figure 48).

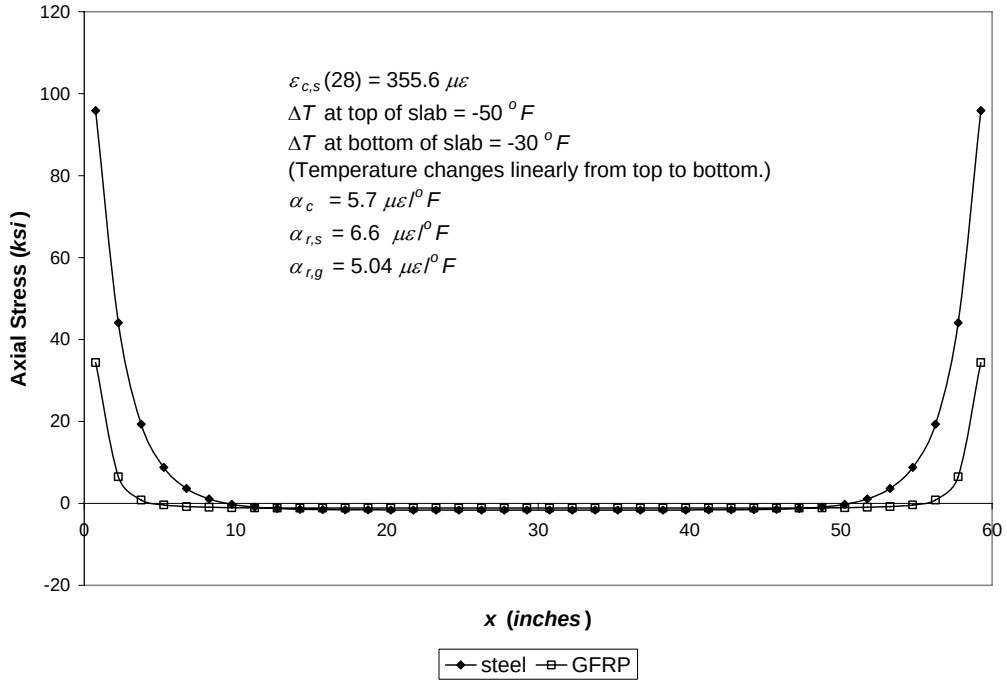

1 inch = 25.4 mm; 1 ksi = 6.89 MPa; 1 (ΔT °F) = 0.56 (ΔT °C); 1 με/°F = 1.80 με/°C

Figure 47. Graph. Axial stress in reinforcement versus longitudinal location of a 1.524-m (5-ft) CRCP segment with ρ = 0.00739 and α_c = 10.26 με/°C (5.7 με/°F).

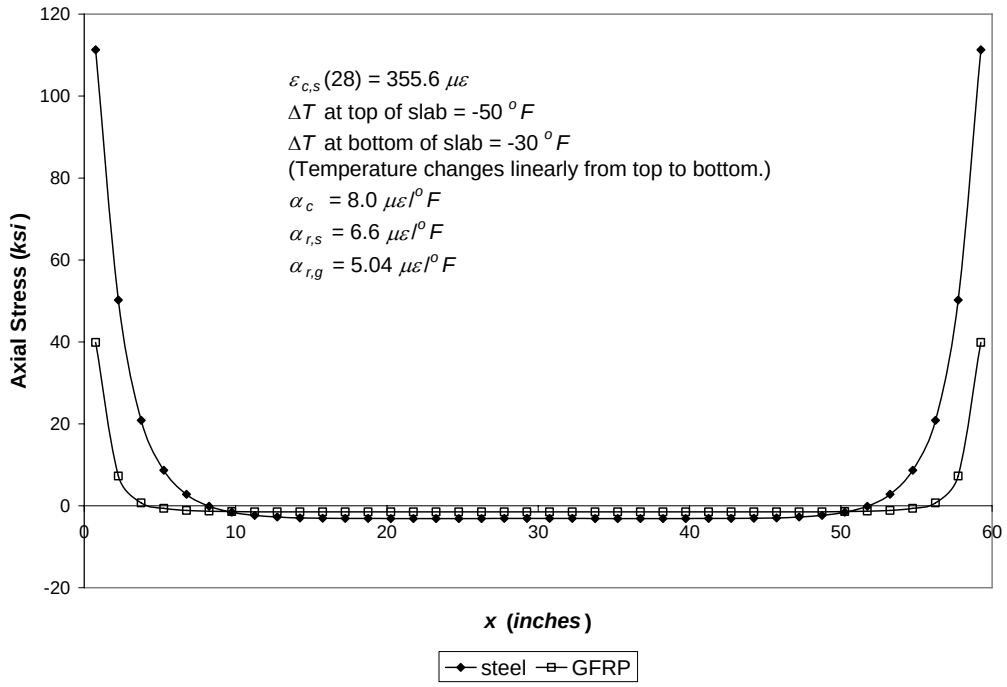

1 inch = 25.4 mm; 1 ksi = 6.89 MPa; 1 (ΔT ^{o}F) = 0.56 (ΔT ^{o}C); 1 με/^{o}F = 1.80 με/^{o}C

Figure 48. Graph. Axial stress in reinforcement versus longitudinal location of a 1.524-m (5-ft) CRCP segment with ρ = 0.00739 and α_c = 14.40 με/^{o}C (8.0 με/^{o}F).

Figures 47 and 48 show that the reinforcements are subjected to higher tensile stresses than the limits of their allowable tensile stresses. While the stress limit for the grade 60 number 6 steel rebar is about 75 percent of its ultimate tensile strength (379 MPa (55 ksi)), the GFRP rebar's allowable tensile stress is about 20 percent of its ultimate tensile strength under a harsh environment (124 MPa (18 ksi)).[2,26] The GFRP rebar's allowable stress range is established for the prevention of any undesired early failure of GFRP rebars under sustained loads due to alkaline attacks on the glass fibers.

Effect of Bond-Slip between Concrete Slab and Subbase

Granite aggregate concrete was adopted for this analysis. The bond between the concrete and reinforcement was again assumed to be perfect, and two different values of the bond-slip between the concrete slab and subbase were considered to study its effect on the stress development and crack width of the 1.524-m (5-ft) GFRP-reinforced CRCP slab segment; the spring stiffnesses used for the slab subbase bonds were 0.236 MN/m (1,350 lbf/inch) and 24.271 MN/m (138,600 lbf/inch). The bond-slip stiffnesses were calculated for the concrete element with a horizontal length of 3.81 cm (1.5 inches) and a thickness of 15.24 cm (6 inches), and simulated for the bond-slip of the concrete slab with respect to the flexible (lime-treated clay) subbase and the cement-stabilized subbase, respectively. While the former was calculated from the bond-slip stiffness per unit area of 40.719 MPa/m (150 lbf/in^2/inch), the latter was calculated from that of 4.180 GPa/m (15,400 lbf/in^2/inch).[33]

Figures 49 and 50 show the FEM results of concrete stresses at the bottom surface and top surface of the GFRP-reinforced concrete pavement along the longitudinal (*x*-) direction, respectively, from varying the bond-slip stiffness between the concrete and subbase. As expected, the maximum tensile stresses in the concrete caused by the shrinkage and temperature variation have drastically increased after considering the aforementioned restraining conditions. Figure 49 shows that the tensile stress in the concrete for the higher subbase friction is larger than that for the lower one at the bottom of the CRCP slab segment. At the top of the slab segment, the reversed result of the concrete stress level has been observed (figure 50); smaller stress was found for the higher friction. The higher subbase friction creates more restraint against the concrete volume change at the bottom of the slab segment. More frictional reaction force is generated at the concrete bottom, leading to less concrete displacement with larger concrete stress at the bottom. Simultaneously, this causes less concrete displacement around the reinforcement and, consequently, less reaction force provided from the reinforcement to the concrete, leading to smaller concrete stresses around the reinforcement and at the top of the slab segment.

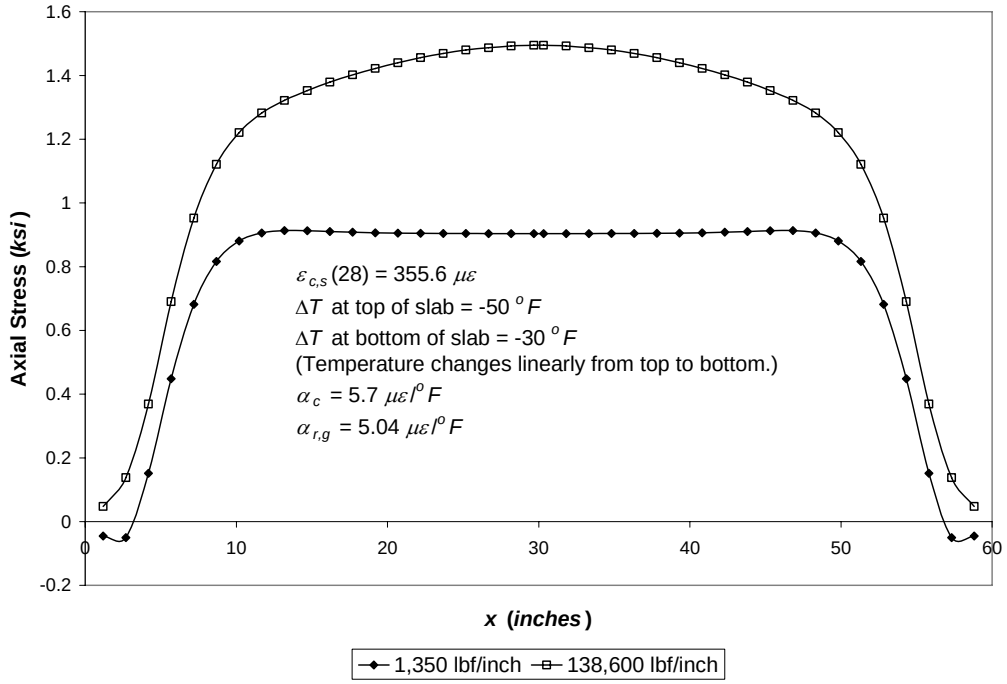

1 inch = 25.4 mm;1ksi = 6.89 MPa; 1(ΔT ^{o}F) = 0.56 (ΔT ^{o}C); 1 με/^{o}F = 1.80 με/^{o}C; 1lbf/inch = 175.12 N/m

Figure 49. Graph. Axial stress at concrete bottom surface versus longitudinal location for two different subbase bond stiffnesses (ρ = 0.00739 and *L* = 1.524 m (60 inches)).

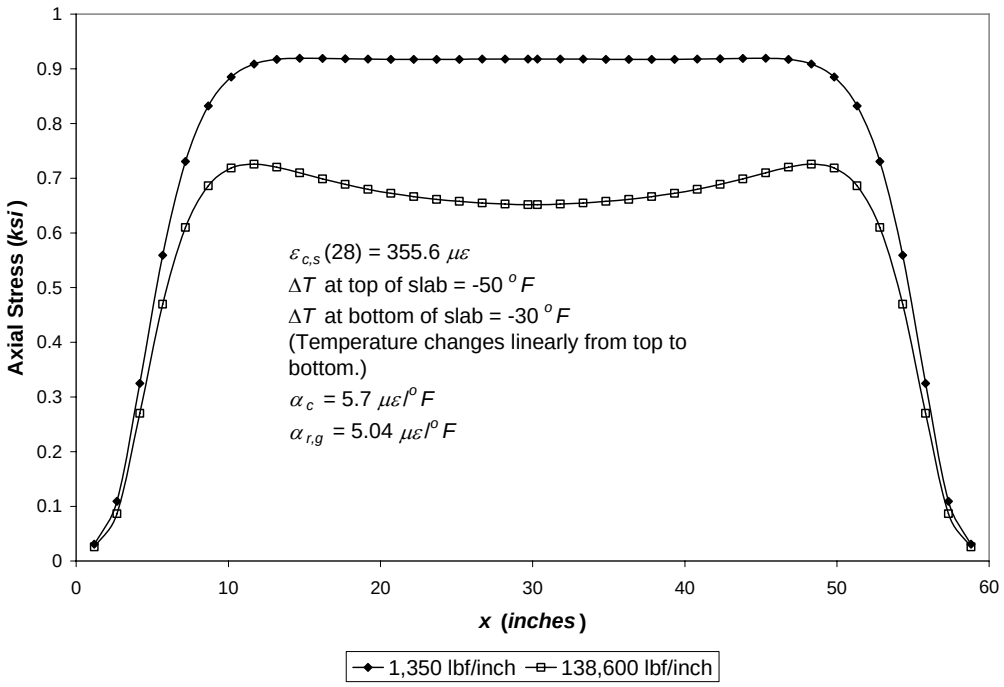

1 inch=25.4 mm;1 ksi=6.89 MPa; 1 (ΔT ^{o}F)=0.56 (ΔT ^{o}C); 1με/^{o}F=1.80 με/^{o}C; 1l bf/inch=175.12 N/m

Figure 50. Graph. Axial stress at concrete top surface versus longitudinal location for two different subbase bond stiffnesses (ρ = 0.00739 and L = 1.524 m (60 inches)).

Figures 51 and 52 show the axial concrete stress contours from the cases employing the two different subbase frictions. Figure 51, representing the lower friction case, shows that the stress variation is almost symmetrical with respect to the longitudinal center line on which the reinforcement is located; the stress contour is similar to that of the case without the subbase friction. On the other hand, the stress in figure 52, for the higher friction case, is observed to drastically change from the bottom to the top of the slab segment; the stress level at the bottom is much higher than that at the top. With such a high subbase friction, the CRCP is likely to have a chance to crack from its bottom area. In addition, the concrete stress at the bottom for the higher friction (figure 50) is larger than that at the top for the lower friction (figure 49). This implies that the CRCP with the higher subbase friction will have more cracks for a certain pavement length, in conjunction with smaller crack spacings. The high stress concentrations are also found around the reinforcement near the crack (the end of the slab segment) in figures 51 and 52.

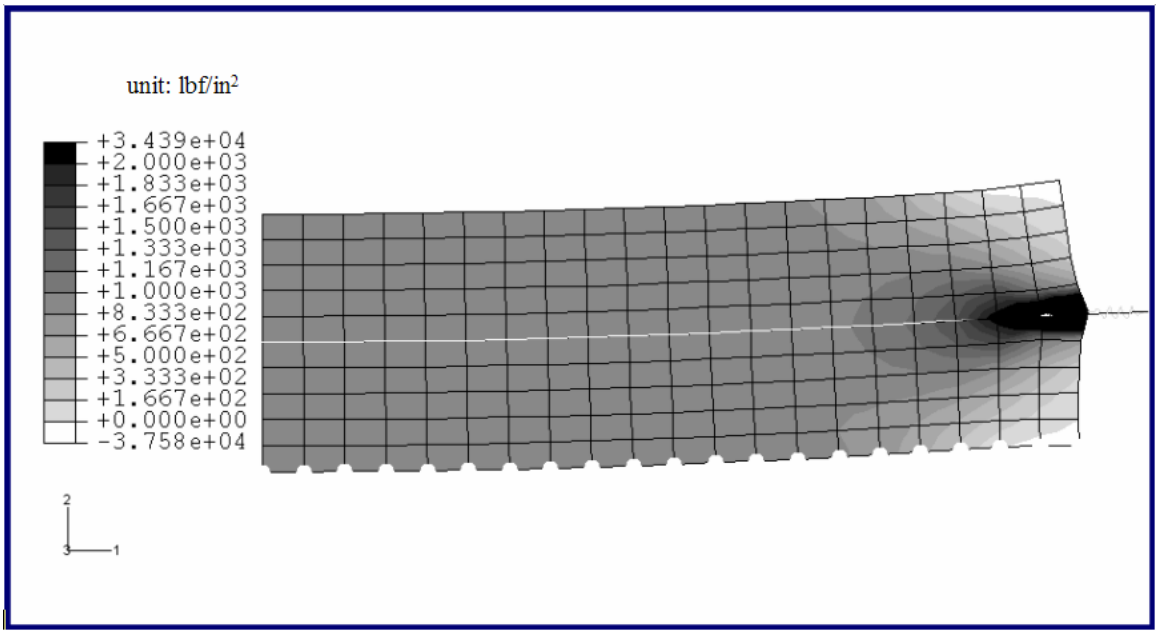

1 lbf/in2 = 6.89 kilopascal (kPa)

Figure 51. Image. Axial stress in concrete versus longitudinal location of a 1.524-m (5-ft) CRCP segment with ρ = 0.00739, α_c = 10.26 με/°C (5.7 με/°F), and a subbase bond-slip stiffness of 0.236 MN/m (1,350 lbf/inch).

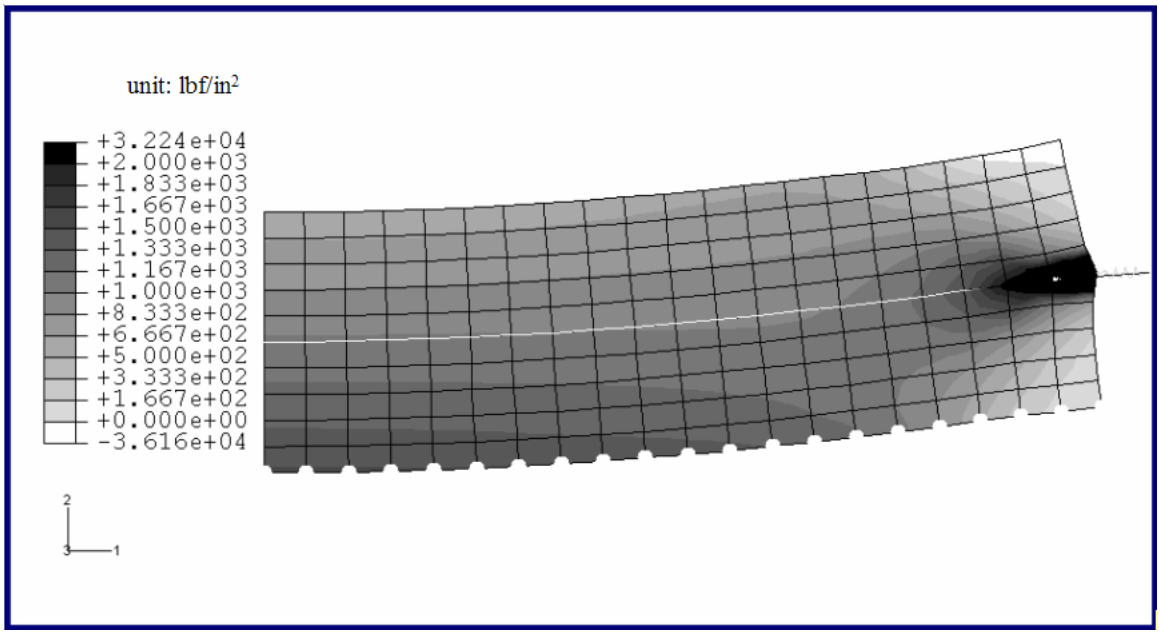

1 lbf/in^2 = 6.89 kPa

Figure 52. Image. Axial stress in concrete versus longitudinal location of a 1.524-m (5-ft) CRCP segment with ρ = 0.00739, α_c = 10.26 με/°C (5.7 με/°F), and a subbase bond-slip stiffness of 24.271 MN/m (138,600 lbf/inch).

The stress distributions in the GFRP reinforcement for the two different subbase frictions are plotted in figure 53. The compressive stresses (negative value in the figure) are developed around the middle of the slab segment in the longitudinal (*x*-) direction for both friction cases. The compressive stress level for the higher friction, about 6.46 MPa (0.94 ksi), is slightly lower than that for the lower friction, about 7.81 MPa (1.13 ksi). At the cracks, a tensile stress of about 222.31 MPa (32.24 ksi) is developed for the higher friction and is also lower than that of about 237.09 MPa (34.39 ksi) for the lower friction. As mentioned before, the subbase with the higher friction applies more frictional reaction force to the bottom of the slab segment as the concrete volume change occurs, leading to less concrete displacements both at the bottom and around the reinforcement. The lesser concrete displacement around the reinforcement releases the force applied to the reinforcement, leading to lower compressive reinforcement stresses around the middle in the longitudinal (*x*-) direction and lower tensile reinforcement stresses at the crack.

The variation of crack width through the depth of the slab segment is observed in figure 54. The crack width at the bottom for the higher friction is narrower than that for the lower friction because of greater restraint from the subbase. The crack width for the higher friction is narrower up to about middepth of the slab (where the reinforcement is located) and becomes wider at the top, presenting more drastic variations through the depth. In the figure, the protrusion on the graph is found at the middepth because of the restraint from the reinforcement, and the crack width at the top of the pavement is shown to be wider than that at the bottom since the magnitude of the temperature drop (ΔT) is larger at the top than at the bottom and the restraint from the subbase exists at the bottom. The crack widths for both cases are below the allowable limitation of 1 mm (0.04 inch).[(2)]

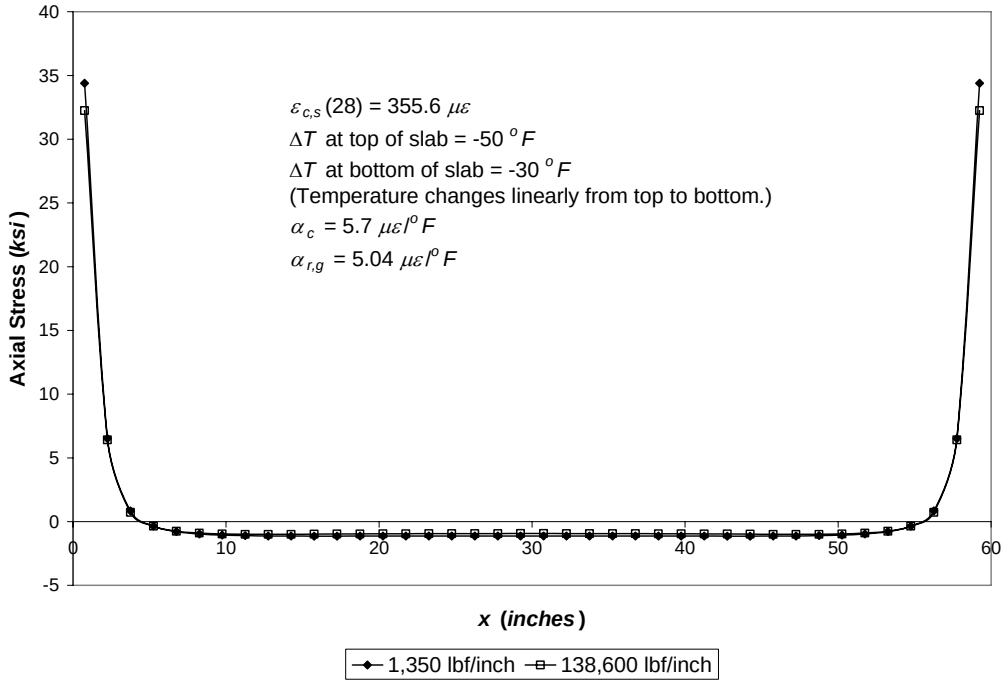

1 inch = 25.4 mm;1 ksi = 6.89 MPa; 1(ΔT ^{o}F) = 0.56 (ΔT ^{o}C); 1$\mu\varepsilon/^{o}$F = 1.80 $\mu\varepsilon/^{o}$C; 1lbf/inch = 175.12 N/m

Figure 53. Graph. Axial stress in GFRP rebar versus longitudinal location for two different subbase bond stiffnesses (ρ = 0.00739 and L = 1.524 m (60 inches)).

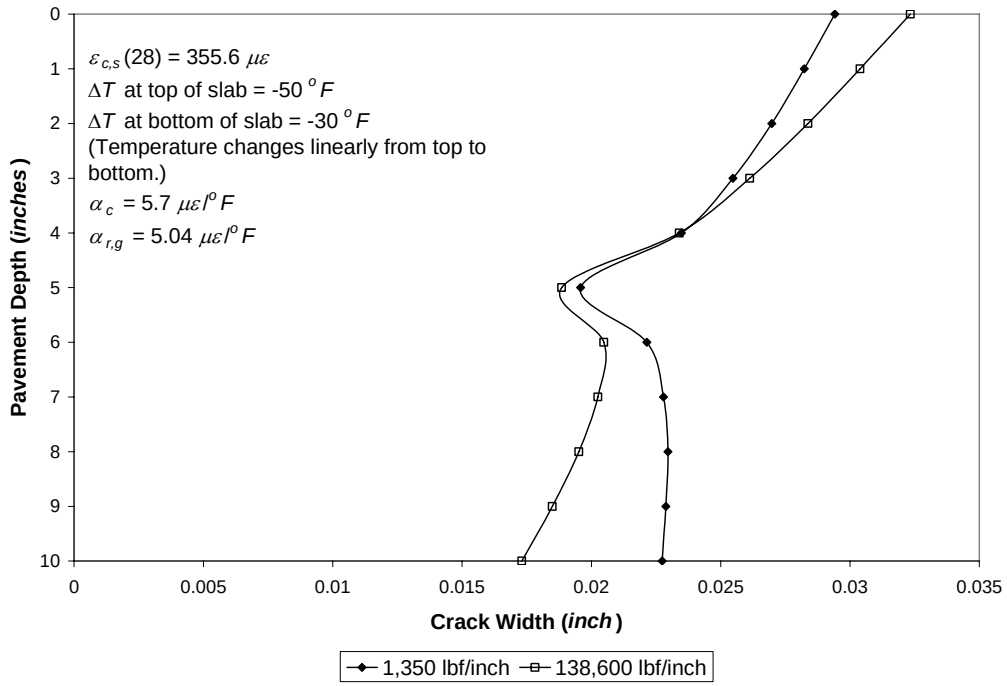

1 inch = 25.4 mm; 1 (ΔT ^{o}F) = 0.56 (ΔT ^{o}C); 1 με/^{o}F = 1.80 με/^{o}C; 1lbf/inch = 175.12 N/m

Figure 54. Graph. Pavement depth versus crack width for two different subbase bond stiffnesses (ρ = 0.00739 and L = 1.524 m (60 inches)).

Effect of Bond-Slip between Concrete and Reinforcement

The FE analysis was also conducted for CRCP slab segments with different bond-slip stiffness between the concrete and the reinforcement. The bond-slip stiffness between concrete and reinforcement varies from 1.344×10^9 N/m (7.675×10^6 lbf/inch), 0.433×10^9 N/m (2.474×10^6 lbf/inch), and 0.175×10^9 N/m (1.0×10^6 lbf/inch), where the first value corresponds to the perfect bond case, the second corresponds to the bond-slip stiffness between the concrete and steel reinforcement, and the third is arbitrarily selected to about 40 percent of the second value. These bond-slip stiffnesses correspond to the bond-slip stiffness per unit area of 589.5×10^3 MPa/m (2.172×10^6 lbf/in^2/inch), 190.0×10^3 MPa/m (0.7×10^6 lbf/in^2/inch), and 76.86×10^3 MPa/m (0.283×10^6 lbf/in^2/inch), respectively. A spring stiffness between the concrete slab and subbase (a flexible subbase or a lime-treated clay subbase) of 236.409 kN/m (1,350 lbf/inch), which corresponds to the bond-slip stiffness per unit area of 40.719 MPa/m (150 lbf/in^2/inch), was applied for the analyses.

Figure 55 shows that the concrete stress level from a larger bond-slip stiffness is higher than that from a smaller stiffness since the tighter bond between the concrete and reinforcement provides more restraint to the concrete's volume change. It can therefore be anticipated that using reinforcement that provides the concrete with a tighter bond can cause more cracks in a certain length of CRCP, leading to smaller crack spacing and a narrower crack width. Under the given conditions, only the maximum concrete stress for the bond-slip stiffness of 0.175×10^9 N/m (1.0×10^6 lbf/inch) is below the tensile

strength of the concrete. Figure 56 shows the axial stress distributions in the GFRP reinforcement for the different bond-slip stiffnesses. The stress level around the crack decreases as the bond-slip stiffness decreases. The tensile stress levels for all the bond-slip cases are higher than the allowable stress limit for the GFRP rebar. Employing reinforcement with a lower bond-slip stiffness might be one way to reduce the stress levels in both concrete and reinforcement in the CRCP. It is noted that the bond between the concrete and GFRP reinforcement cannot be perfect, and for practical purposes it can be assumed to be between the second and third bond cases. Stress development in the CRCP is sensitive to the bond between the concrete and the reinforcement.

The variation of crack width throughout the pavement depth for the crack spacing, *L*, of 1.524 m (5 ft) is shown in figure 57. The crack width for the higher bond-slip stiffness is narrower than that for the lower ones as a result of having more restraint against the concrete volume change. Also, the crack width for steel reinforcement is narrower than that for GFRP reinforcement at a bond-slip stiffness due to the higher Young's modulus of the steel reinforcement.

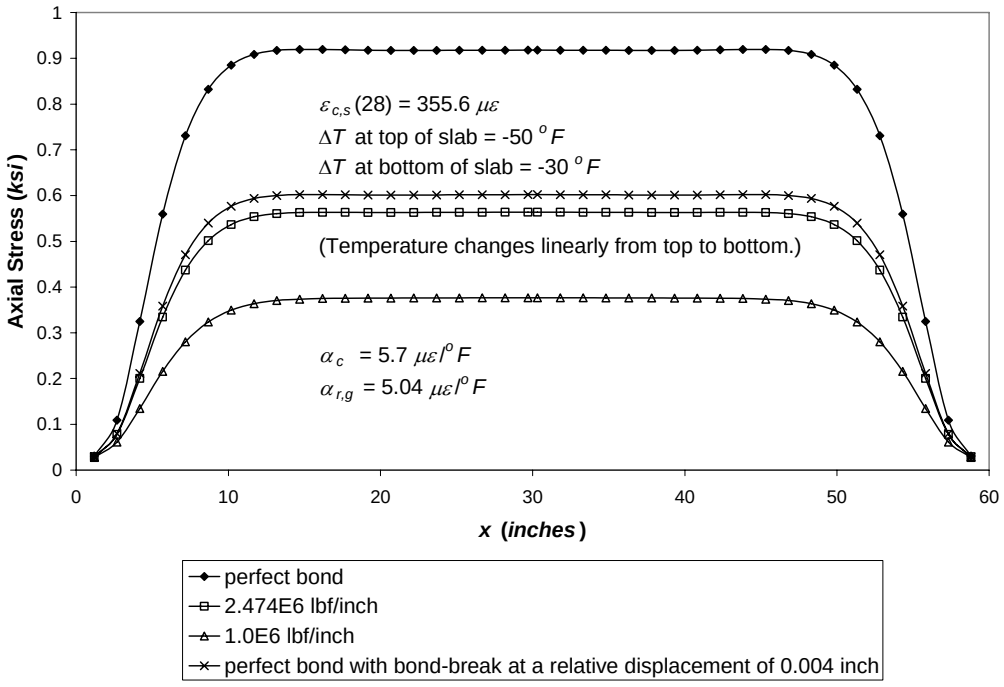

1 inch=25.4 mm; 1 ksi=6.89 MPa; 1 (ΔT ^{o}F)=0.56 (ΔT ^{o}C); 1 με/^{o}F=1.80 με/^{o}C; 1 lbf/inch=175.12 N/m

Figure 55. Graph. Axial tensile stress on concrete surface versus longitudinal location for different bond-stiffnesses (ρ = 0.00739 and *L* = 1.524 m (60 inches)).

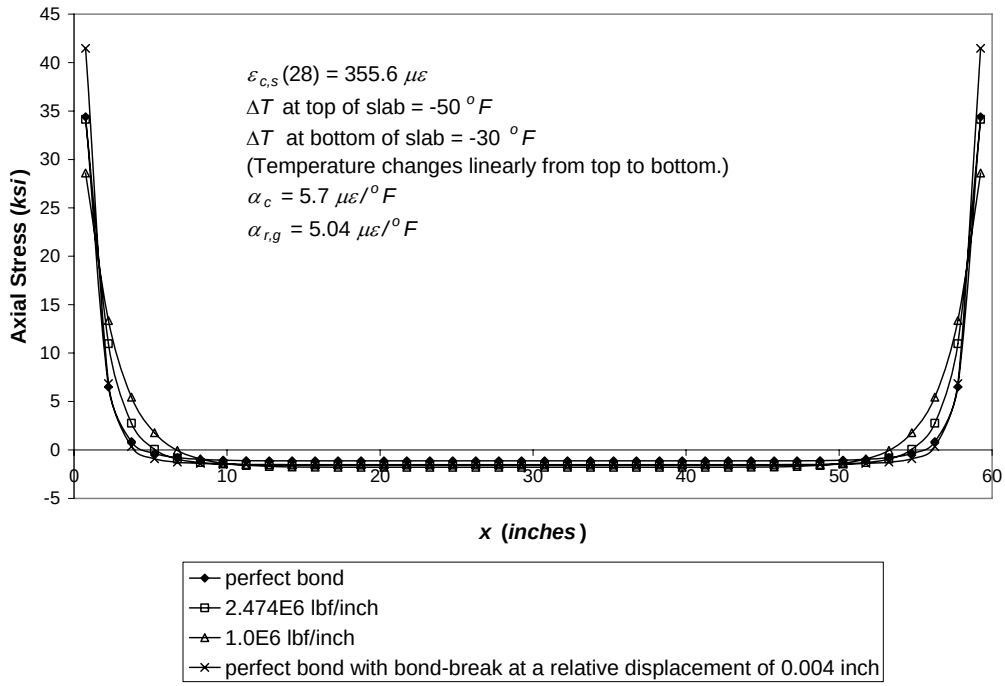

1 inch=25.4 mm; 1 ksi=6.89 MPa; 1 (ΔT ^{o}F)=0.56 (ΔT ^{o}C); 1 με/^{o}F=1.80 με/^{o}C; 1 lbf/inch=175.12 N/m

Figure 56. Graph. Axial stress in GFRP rebar versus longitudinal location for different bond-stiffnesses (ρ = 0.00739 and L = 1.524 m (60 inches)).

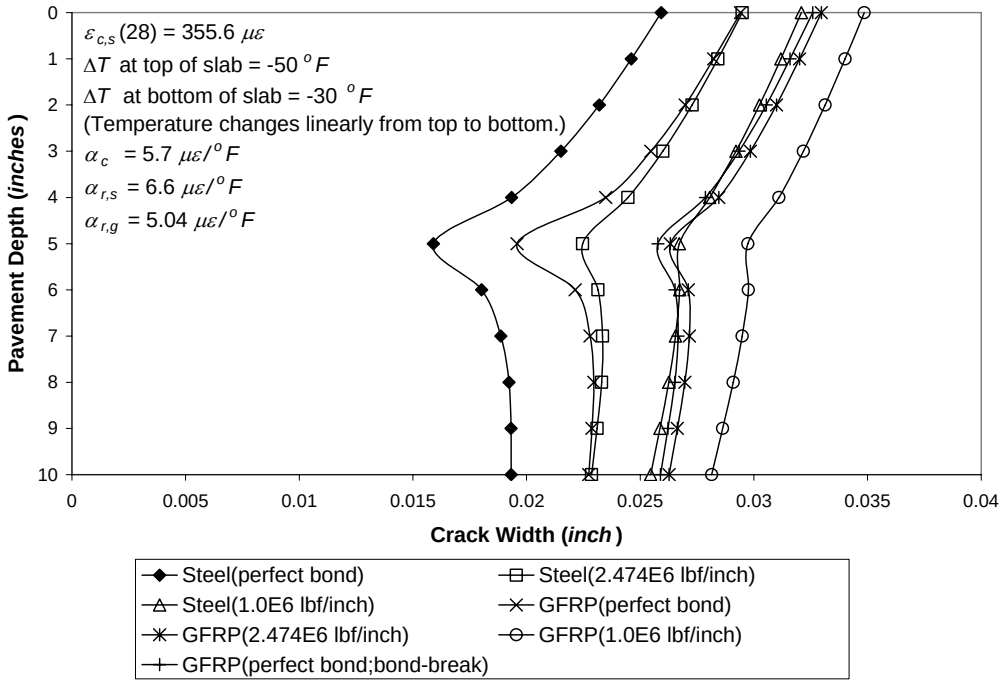

1 inch = 25.4 mm; 1 (ΔT ^{o}F) = 0.56 (ΔT ^{o}C); 1 με/^{o}F = 1.80 με/^{o}C; 1 lbf/inch = 175.12 N/m

Figure 57. Graph. Pavement depth versus crack width for different bond stiffnesses (ρ = 0.00739 and L = 1.524 m (60 inches)).

In figure 57, the protrusions on the graph are found at the middepth of the pavement (where the reinforcement is located), and the graph is observed to be more protruded with the higher bond-slip stiffness. This results from the fact that the concrete volume change is restrained most at the middepth by the reinforcement and is subjected to more restraint as the bond-slip stiffness increases. The crack width at the top of the pavement is wider than that at the bottom of the pavement since the magnitude of the temperature drop (ΔT) is larger at the top than at the bottom, and the restraint from the subbase exists at the bottom. The crack widths throughout the pavement depth for all the cases are below 1 mm (0.04 inch), which is the assumed maximum allowable crack width to prevent the loss of concrete aggregate interlock.

The high stress concentration caused by the perfect bond assumption between the concrete and reinforcement, as found around the reinforcement near the crack in figures 51 and 52, is not realistic; the bond between the concrete and reinforcement will actually break near the crack, relieving the stress concentration as shown in figure 58, whose FE model is equivalent to that of figure 51 except that the bond-slip springs between concrete and reinforcement are modeled to yield when the relative spring displacement between concrete and reinforcement exceeds 0.1 mm (0.004 inch). The calculated bond-break appears at the first spring element; hence, the bond-break length is less than 3.81 cm (1.5 inches) starting from the surface of the crack. The bond-break near the crack also lowers the overall stress level in concrete (as shown in figure 58).

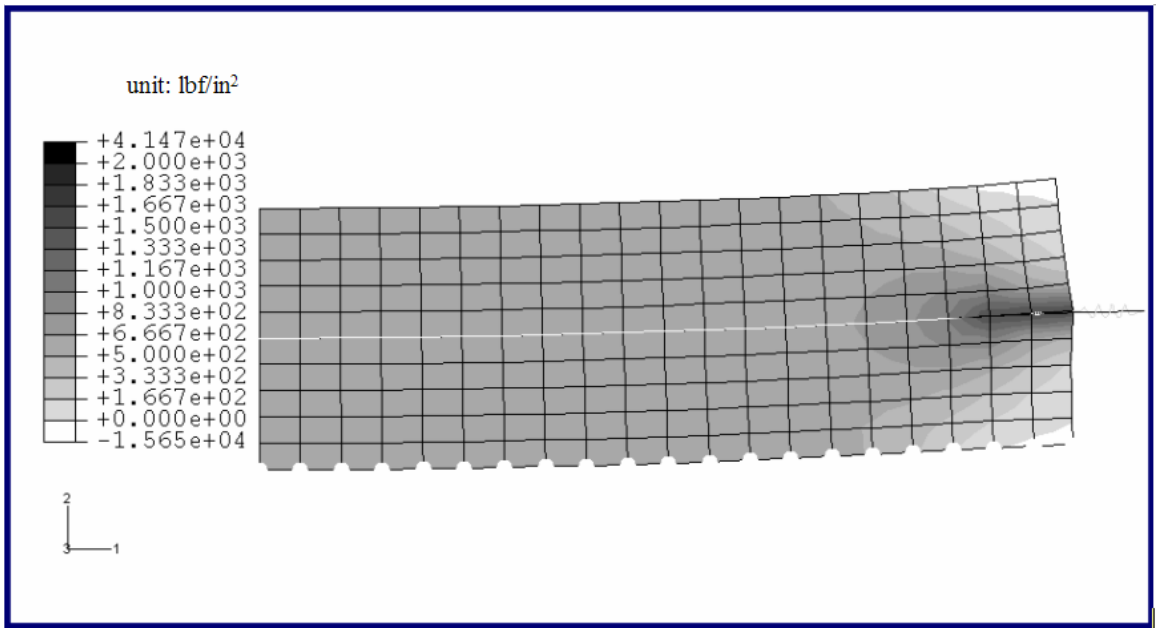

1 lbf/in^2 = 6.89 kPa

Figure 58. Image. Axial stress in concrete versus longitudinal location of a 1.524-m (60-inch) CRCP segment with ρ = 0.00739, α_c = 10.26 με/°C (5.7 με/°F), and a subbase bond-slip stiffness of 236.409 kN/m (1,350 lbf/inch; bond-break considered).

This effect of bond-break can also be seen in figures 55 and 56. While the bond-break near the crack decreases the tensile concrete stress from about 6.33 MPa (0.92 ksi) to 4.15 MPa (0.60 ksi) on the concrete surface, it increases the tensile reinforcement stress from about 237.09 MPa (34.39 ksi) to 285.94 MPa (41.47 ksi) at the cracks, and the compressive reinforcement stress from about 7.81 MPa (1.13 ksi) to 10.49 MPa (1.52 ksi) at the midspan. If bond-break length increases, which will make more spring elements yield, the maximum tensile stress in the reinforcement will reduce. In addition, the effect of the bond-break on the crack width variation in the case of GFRP reinforcement is shown in figure 57. Since the bond breaks near the crack, the crack widths throughout the pavement depth become wider than those without the bond-break assumption; note that the maximum crack width of the 1.524-m (5-ft) CRCP segment is about 0.83 mm (0.033 inch) on the top surface, which is just under the allowable crack width limitation, 1 mm (0.04 inch).

FE ANALYSIS OF CRCP SEGMENTS WITH DIFFERENT LENGTHS

The previous FE results show that, in most cases, not only do the concrete stresses exceed the concrete tensile strength, but the reinforcement stresses around the crack also exceed the limit of allowable working stress of GFRP rebar under the given conditions. As previously shown, the lower bond-slip stiffness between concrete and reinforcement, as well as the smaller CTE and Young's modulus of concrete, can lower the stress levels in the concrete and reinforcement. Therefore, the bond-slip stiffness of 0.433×10^9 N/m (2.474×10^6 lbf/inch), instead of perfect bond, is employed for a design example, along with a concrete CTE of 6.84 με/°C (3.8 με/°F) and Young's modulus of 24.8 GPa (3.6×10^6 lbf/in^2) for a limestone aggregate concrete. The bond-slip stiffness between concrete and subbase for flexible subbase (or lime-treated clay subbase) is applied for the example. In addition, the CRCP segments at three different lengths—1.067 m (3.5 ft), 1.524 m (5 ft), and 2.438 m (8 ft)—are modeled to represent the range of the crack spacing anticipated from the conventional CRCP design, which is 1.067 to 2.438 m (3.5 to 8.0 ft). The other conditions for the example are the same as previously adopted.

The axial tensile concrete stress distribution at the top of the slab segment, along the longitudinal direction, has been plotted for each slab length (figure 59). As shown in the figure, the concrete stress level of the longer slab segment is higher than that of the shorter slab segment. The maximum stress levels in the concrete for the lengths of 1.067 m (3.5 ft), 1.524 m (5 ft), and 2.438 m (8 ft) are about 1.86 MPa (270 lbf/in^2), 3.08 MPa (447 lbf/in^2), and 6.16 MPa (893 lbf/in^2), respectively. The stress level for L = 2.438 m (8 ft) is well above the tensile strength, about 2.41 MPa (350 lbf/in^2), of the limestone concrete approximated with a concrete compressive strength, f_c', of about 27.58 MPa (4,000 lbf/in^2). This slab segment will crack at the middle. On the other hand, the slab segments with lengths shorter than 1.067 m (3.5 ft) will not crack at the middle; the maximum stress level for L = 1.067 m (3.5 ft) does not reach the tensile strength of concrete. The stress level for L = 1.524 m (5 ft) is assumed to be roughly on the verge of the cracking point or has slightly passed the point. Therefore, the crack spacing for the example is anticipated to be between 1.067 m (3.5 ft) and 1.524 m (5 ft).

Figure 60 shows the axial stress distributions in the GFRP reinforcement for the different slab segment lengths. Around the crack, the stress levels in the GFRP reach around 113.83 MPa (16.51 ksi), 192.70 MPa (27.95 ksi), and 387.59 MPa (56.21 ksi) for the lengths of 1.067 m (3.5 ft), 1.524 m (5 ft), and 2.438 m (8 ft), respectively. Except for the case of L = 1.067 m (3.5 ft), the GFRP reinforcement is subjected to higher stress levels than its limit of allowable tensile stress (124 MPa; 18 ksi); with the anticipated crack spacing of this example, shorter than 1.524 m (5 ft), the stress level could meet its limit. The variation of crack width along the pavement depth is shown in figure 61. The crack width for the longer slab segment is wider than that for the shorter one. Except for the case of L = 2.438 m (8 ft), the crack widths for all cases are below the limit of allowable crack width, 1 mm (0.04 inch).

It can be understood in this chapter that the behavior of the CRCP can be adjusted by varying the concrete material properties, subbase type, and the bond characteristics between concrete and reinforcement. For example, if it is necessary to have a smaller crack spacing in the CRCP (which can be attained by creating higher concrete stress level), concrete with a larger CTE and Young's modulus, a subbase providing the concrete slab with higher friction, reinforcement which bonds better with concrete, or a combination of the three may need to be employed. This study reveals that careful consideration of these parameters can provide favorable control of the stresses in the concrete and reinforcement followed by the control of cracking in the CRCP, allowing for a sound design of the GFRP-reinforced CRCP.

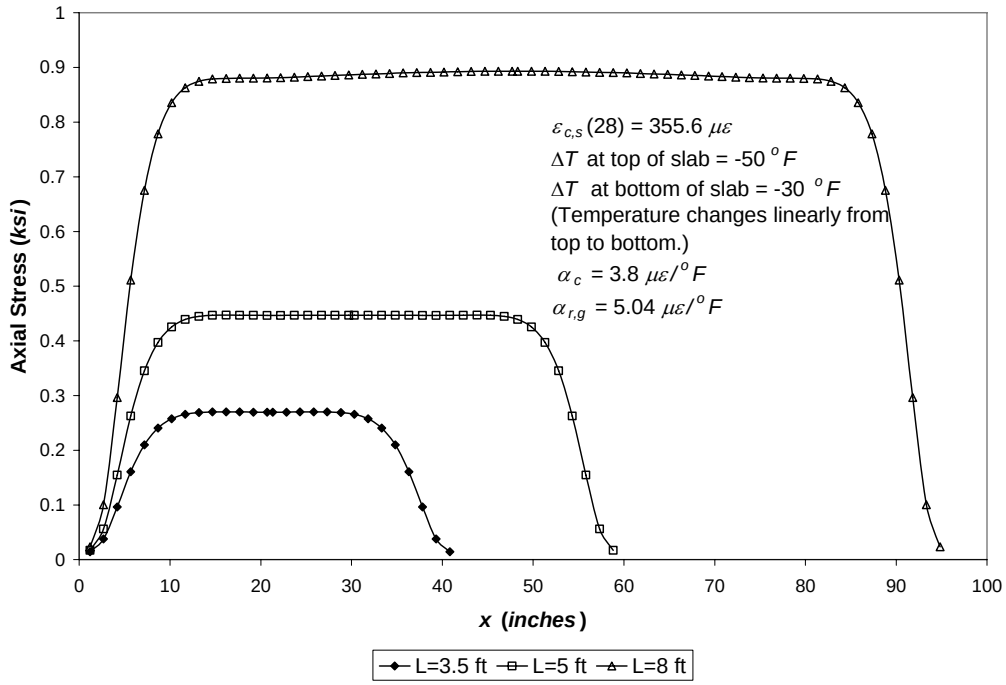

1 inch = 25.4 mm; 1 ksi = 6.89 MPa; 1 (ΔT ^oF) = 0.56 (ΔT ^oC); 1 $\mu\varepsilon/^oF$ = 1.80 $\mu\varepsilon/^oC$; 1 ft = 0.305 m

Figure 59. Graph. Axial tensile stress on concrete surface versus longitudinal location for different slab segment lengths (ρ = 0.00739; bond-slip stiffness = 0.433 × 10^9 N/m (2.474 × 10^6 lbf/inch)).

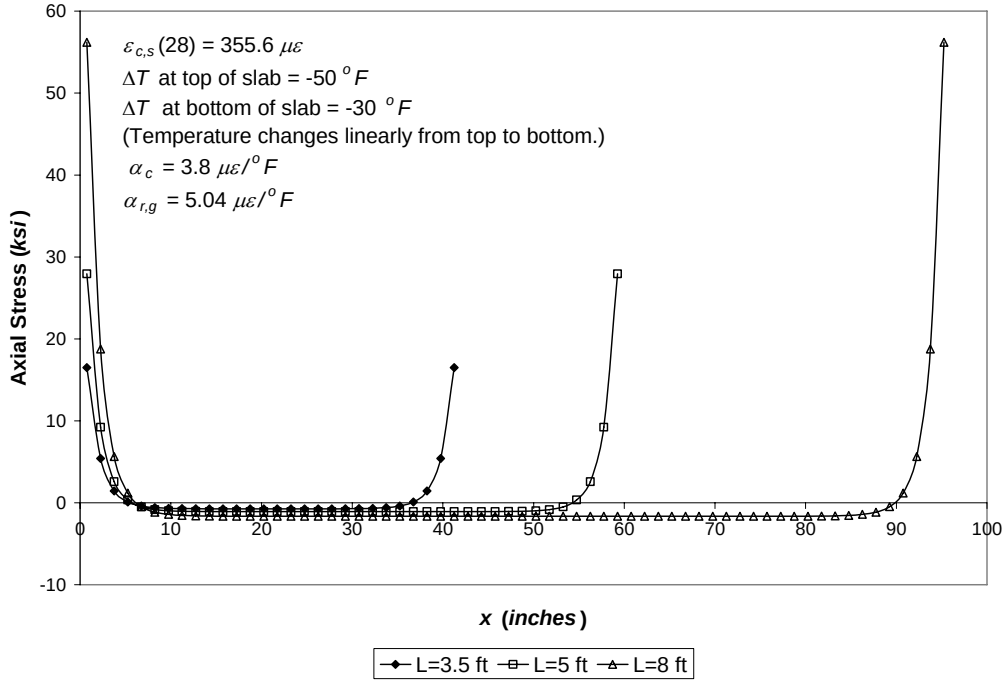

1 inch = 25.4 mm; 1 ksi = 6.89 MPa; 1 (ΔT °F) = 0.56 (ΔT °C); 1 με/°F = 1.80 με/°C; 1 ft = 0.305 m

Figure 60. Graph. Axial stress in GFRP rebar versus longitudinal location for different slab segment lengths (ρ = 0.00739; bond-slip stiffness = 0.433 × 10^9 N/m (2.474 × 10^6 lbf/inch)).

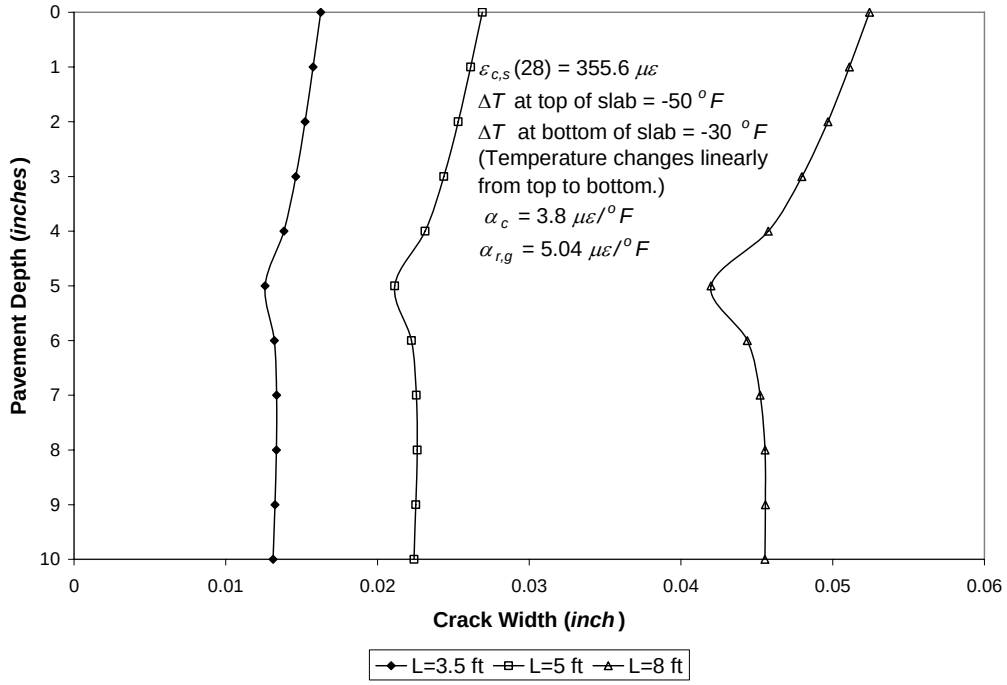

1 inch = 25.4 mm; 1 (ΔT °F) = 0.56 (ΔT °C); 1 με/°F = 1.80 με/°C; 1 ft = 0.305 m

Figure 61. Graph. Pavement depth versus crack width for different slab-segment lengths (ρ = 0.00739; bond-slip stiffness = 0.433 × 10^9 N/m (2.474 × 10^6 lbf/inch)).

Design considerations related to crack spacing (1.067 to 2.438 m; 3.5 to 8 ft), crack width limitation (≤1 mm (0.04 inch)), and the allowable stress limit of GFRP reinforcement were also presented in this chapter, and the results indicated that GFRP-reinforced CRCP can satisfy these requirements. For cost considerations, the reinforcement amount used in the proposed design (≈0.74 percent) was chosen to be the same as a traditional steel-reinforced CRCP. Typical reinforcement amounts for steel-reinforced CRCP can range between 0.5 and 0.7 percent, depending on the weather conditions.[20] Increasing the reinforcement amount will reduce the reinforcement stress, which may be a simple and necessary consideration for the GFRP-reinforced CRCP when the pavement is likely to be subjected to a harsh environment with high temperature variations and alkaline attack.

The current design example using number 6 rebars at 15.2-cm (6-inch) spacing in the longitudinal direction and number 5 at 121.9-cm (4-ft) spacing in the transverse direction in a 3.658-m- (12-ft) wide lane shows feasible performance under an extreme temperature variation (ΔT = –27.8 °C (–50 °F) at the top surface of the pavement and ΔT = –16.7 °C (–30 °F) at the bottom surface), with a concrete shrinkage of 355.6 με at 28 d. By careful consideration of concrete properties, proper bond between GFRP rebar and concrete, reinforcement amount, and subbase friction, the above design shows satisfactory performance.

CHAPTER 6. MECHANISTIC STUDY OF GFRP-CRCP DESIGN

DESIGN INFORMATION OF STEEL-CRCP AND GFRP-CRCP FOR MECHANISTIC ANALYSIS

The Virginia Department of Transportation planned to construct a steel-reinforced CRCP on S.R. 288 in June 2003.[12] The CRCP would consist of two lanes: one 4.267-m- (14-ft-) wide travel lane, and a 3.658-m- (12-ft-) wide passing lane. The CRCP section is 25.4 cm (10 inch) thick, and it is reinforced with a steel reinforcing ratio of about 0.74 percent, which corresponds to number 6 longitudinal reinforcements spaced at 15.24 cm (6 inches). Number 5 steel rebars were used for the transverse reinforcement at a spacing of 121.9 cm (48 inches). Below the pavement section is a 7.62-cm- (3-inch-) thick asphalt-stabilized open graded drainage layer (OGDL; number 57 AASHTO gradation, treated with 2.5 percent asphalt by weight), which is then supported by a 15.24-cm- (6-inch-) thick layer of cement-treated aggregate (dense aggregate type I, size 21A, treated with 4 percent cement by weight). The coarse aggregate of metamorphosed granite is used for concrete mix. The design parameters and material properties of the VDOT's CRCP are listed in table 5; the table also includes the GFRP material properties and the assumed bond property between concrete and subbase for the following mechanistic study of a GFRP-reinforced CRCP.

The performance of the steel-reinforced CRCP at 28 d in terms of crack spacing, crack width, and tensile stress level in steel reinforcement at crack was predicted by using the mechanistic analysis program, CRCP8.[22] A mean crack spacing of 1.058 m (3.47 ft), a crack width of 0.49 mm (0.0193 inch), and a reinforcement tensile stress at crack of 288.56 MPa (41.850 ksi) were obtained. The crack spacing is acceptable even though the crack spacing of 1.058 m (3.47 ft) barely meets its allowable lower limit of 1.067 m (3.5 ft) since the punchout failure, which is first characterized by a loss of aggregate interlock at one or two closely spaced cracks (usually less than 0.610 m (2 ft)), can be avoided provided that the crack width is narrow enough ($\leq$ 1 mm (0.04 inch)).[2,10] Also, the steel reinforcement stress at crack is lower than its maximum allowable limit of 379 MPa (55 ksi), which is about 75 percent of the ultimate tensile strength for the grade 60 number 6 steel rebar.[2]

In the following section, based on the design parameters and material properties of VDOT's CRCP (table 5), except for replacing number 6 steel reinforcement with number 6 GFRP reinforcement, the performance of GFRP-reinforced CRCP will be predicted over various types of concrete and subbase. This mechanistic prediction shows the effect of using different types of concretes and subbases on the pavement's performance, which the FE analysis previously conducted could not explicitly indicate. In addition, the performance of the GFRP-CRCP will be compared with that of the steel-CRCP in this chapter. The ideal situation is to come up with a feasible GFRP-CRCP design that performs comparable to the steel-CRCP without raising the GFRP reinforcement ratio. Considered in the mechanistic simulation of GFRP-CRCP is also the same GFRP rebar properties utilized in the FE analysis in Chapter 5.

Table 5. Design parameters and material properties used in mechanistic analysis.

Parameters and Properties[1]	Value
Longitudinal reinforcement spacing (cm (inches))	15.24 (6.0)
Pavement thickness (cm (inches))	25.4 (10.0)
Young's modulus of concrete at 28 d (GPa (× 10^6 lbf/in^2))	31.44 (4.56)
Compressive strength of concrete at 28 d (MPa (lbf/in^2))	32.13 (4,660)
Tensile strength of concrete at 28 d (MPa (lbf/in^2))	3.86 (560)
Total shrinkage of concrete (με)	394
Young's modulus of steel rebar (GPa (× 10^6 lbf/in^2))	200.00 (29)
Longitudinal Young's modulus of GFRP rebar (GPa (× 10^6 lbf/in^2))	41.37 (6.0) (≈40.80 (5.92))
Ultimate tensile strength of GFRP rebar (MPa (ksi))	620 (90)
CTE of concrete, α_c (με/^{o}C (με/^{o}F))	10.33 (5.74)
CTE of steel rebar, $\alpha_{r,s}$ (με/^{o}C (με/^{o}F))	11.88 (6.6)
CTE of GFRP rebar, $\alpha_{r,g}$ (με/^{o}C (με/^{o}F))	9.07 (5.04)
Bond-slip stiffness/unit area bet. concrete and subbase (MPa/m (lbf/in^2/inch))	15.17 (55.88)
Curing, minimum temperature (^{o}C (^{o}F))	43.3 (110), –3.89 (25)
Static single wheel load (kg (lb)), wheel base radius (cm (inches))	4,540 (10,000), 15.24 (6.0)

[1]Granite aggregate is used for concrete mix; number rebar is considered; asphalt-stabilized subbase is used.

CRACK DEVELOPMENT AND REINFORCEMENT STRESS IN GFRP-CRCP WITH VARYING CONCRETE COARSE AGGREGATE TYPE

The material properties of concrete (such as CTE and Young's modulus) are primarily a function of the type of coarse aggregate, and since these properties are interdependent, a consistent set of properties that are representative of the concrete mixture to be used should be carefully selected for the concrete pavement design and analysis.[30] The approximate sets of concrete material properties are listed in table 6. Except for that of granite concrete, the compressive strengths are assumed to be 31.03 MPa (4,500 lbf/in^2) to approximate the values of indirect tensile strength, followed by the flexural strength and drying shrinkage values. The concrete material properties and their approximate relationship have been identified by other researchers.[30] In table 6, it is shown that the coarse aggregate types are listed in order of lowest to highest concrete CTE, which are 6.84 με/^{o}C (3.8 με/^{o}F) for limestone concrete and 14.40 με/^{o}C (8.0 με/^{o}F) for siliceous river gravel concrete, respectively.

Table 6. Concrete material properties at 28 d used in mechanistic analysis (varied by using different types of coarse aggregate). [30]

Coarse Aggregate Type	Coefficient of Thermal Expansion ($\mu\varepsilon/^oF$[1])	Compressive Strength (lbf/in^2 [2])	Young's Modulus ($\times 10^6$ lbf/in^2)	Tensile Strength (lbf/in^2)	Flexural Strength (lbf/in^2)	Drying Shrinkage ($\mu\varepsilon$)
Limestone	3.8	4,500	3.6	387	625	626
Basalt	4.8	4,500	3.8	486	992	471
Granite	5.74	4,660	4.56	560	610	394
Dolomite	5.9	4,500	4.8	495	895	458
Sandstone	6.5	4,500	3.8	468	762	498
Quartz	6.6	4,500	4.5	495	868	458
Siliceous River Gravel	8.0	4,500	5.0	419	697	572

[1] 1 $\mu\varepsilon/^oF$ = 1.80 $\mu\varepsilon/^oC$.
[2] 1 lbf/in^2 = 0.00689 MPa.

Figure 62 shows the prediction of mean crack spacing for the GFRP-CRCP over various types of concrete coarse aggregate as well as that for the steel-GFRP with granite coarse aggregate, which is the VDOT's CRCP. It can be easily understood that the GFRP-CRCP with granite concrete has larger crack spacing (2.115 m (6.94 ft)) than does the VDOT's steel-CRCP (1.058 m (3.47 ft)) since the Young's modulus of GFRP is smaller than that of steel. Among the GFRP-CRCPs, the CRCP using basalt concrete is predicted to have the largest crack spacing of 2.457 m (8.06 ft), which slightly exceeds the upper limit of allowable crack spacing of 2.438 m (8 ft). This is reasonable since the basalt concrete has a relatively low CTE and Young's modulus, which cause low tensile stress development in concrete and result in less cracks in the CRCP. On the other hand, using the siliceous river gravel concrete creates the smallest crack spacing of 1.003 m (3.29 ft), which results from its high CTE, high Young's modulus, and large shrinkage; this is still acceptable, despite slightly deviating from the lower allowable limit of 1.067 m (3.5 ft) for reasons discussed at the beginning of this chapter.

It is found in the prediction that even though the limestone concrete has the lowest CTE and Young's modulus, the crack spacing is smaller than those for the basalt, granite, dolomite, and quartz concretes (a result of this type having the lowest tensile strength and largest shrinkage). It can therefore be understood that the material properties of each type of concrete must be collectively considered and used in the CRCP design. From the comparison in crack spacing between the GFRP-CRCPs and VDOT's steel-CRCP, it is

also found that the GFRP-CRCPs using the sandstone and the siliceous river gravel concretes have crack spacings comparable to that for VDOT's steel-CRCP without increasing the amount of GFRP reinforcement. In addition to the comparable GFRP-CRCPs, the GFRP-CRCP using the limestone concrete has a crack spacing of 1.814 m (5.95 ft), which is within the acceptable range for the criteria of crack spacing.

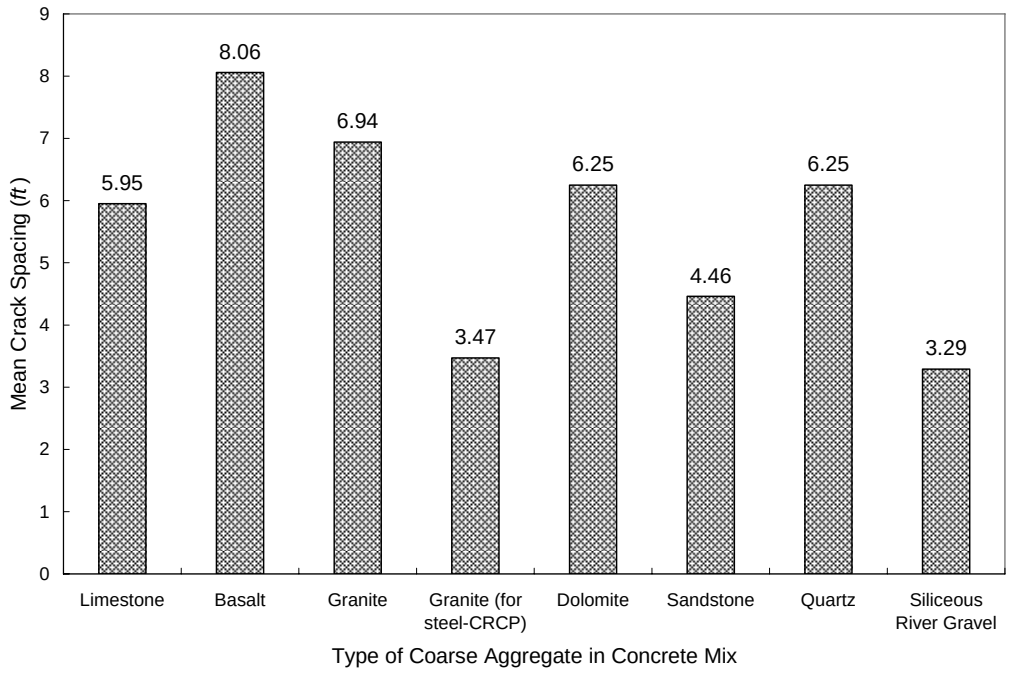

1 ft = 0.305 m

Figure 62. Graph. Mean crack spacing versus type of coarse aggregate in concrete mix (ρ = 0.0074; asphalt-stabilized subbase).

In figure 63, the crack widths were predicted and compared over various concrete coarse aggregate types. In general, the crack widths appear to be wider as their corresponding crack spacings are larger. Also, a larger volume change in concrete appears to contribute to developing a wider crack width. The comparison in crack widths between the limestone and siliceous river gravel cases shows that the crack width for the limestone case, 0.54 mm (0.0211 inch), is narrower than that for the siliceous river gravel case, 0.67 mm (0.0263 inch), although the crack spacing for the limestone case, 1.814 m (5.95 ft), is larger than that for the siliceous river gravel case, 1.003 m (3.29 ft). This can be explained by considering the much larger concrete volume change of siliceous river gravel concrete, which is mainly induced by its much higher CTE. The same explanation can be applied to the comparison between the dolomite and quartz cases.

Among all crack widths which meet the maximum limiting criteria of ≤ 1 mm (0.04 inch), the crack widths for the limestone, sandstone, and siliceous river gravel cases can provide a reliable concrete aggregate interlock at crack. In addition, tighter cracks can be

generally expected with the steel reinforcement, since the steel reinforcement (having a higher Young's modulus) can better restrain the concrete volume change and hold the crack more tightly.

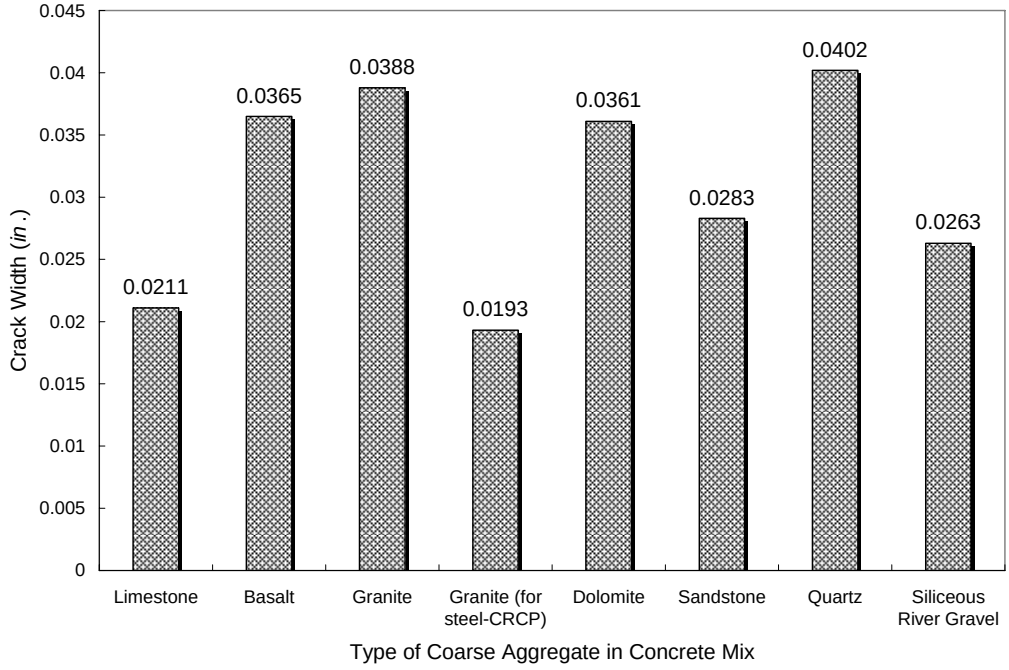

1 inch = 25.4 mm

Figure 63. Graph. Crack width versus type of coarse aggregate in concrete mix (ρ = 0.0074; asphalt-stabilized subbase).

Figure 64 shows the tensile stress level in reinforcement at crack for various types of concrete coarse aggregate. The tensile stress levels in GFRP reinforcement are in the range of about 137.90 to 172.38 MPa (20 to 25 ksi), levels that are somewhat higher than the GFRP rebar's allowable tensile stress limit of 124 MPa (18 ksi), which is about 20 percent of its ultimate tensile strength under a harsh environment; this adverse result could be resolved by using a new type of GFRP rebar such as alkaline-resistant GFRP rebar (such as Advantex™ glass GFRP) which has an allowable stress limit that can be higher than 20 percent.[26] The stress levels in GFRP reinforcement appear to correlate with their corresponding crack widths. In the case of steel-CRCP, the reinforcement stress level is 288.56 MPa (41.850 ksi), which is lower than its limit of 379 MPa (55 ksi) and about 75 percent of the ultimate tensile strength of steel rebar.[2] The higher reinforcement stress for steel-CRCP is attributed to the higher Young's modulus of steel.

From the results, any of the GFRP-CRCPs with the limestone, sandstone, and siliceous river gravel concrete seems to perform satisfactorily without raising the reinforcement ratio under the given conditions provided by VDOT design data. In addition, even though the results show that the GFRP-CRCP with the granite concrete can satisfy the limiting

criteria, one may still want to increase the reinforcement ratio to avoid the possibility of violating the limiting criteria due to environmental variations.

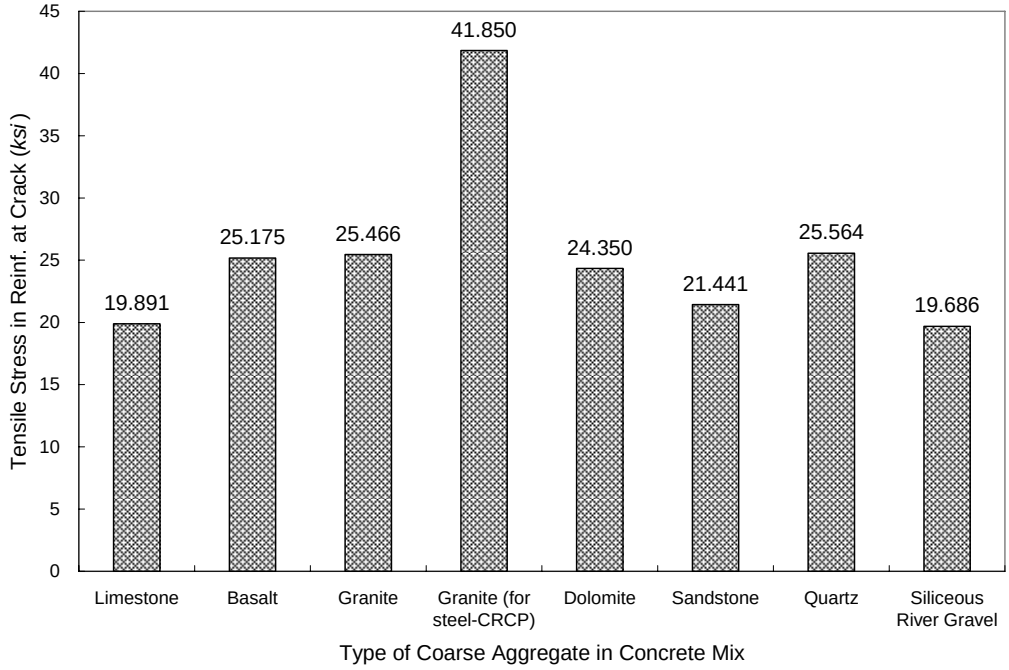

1 ksi = 6.89 MPa

Figure 64. Graph. Tensile stress in reinforcement at crack versus type of coarse aggregate in concrete mix (ρ = 0.0074; asphalt-stabilized subbase).

CRACK DEVELOPMENT AND REINFORCEMENT STRESS IN GFRP-CRCP WITH VARYING SUBBASE TYPE

The comparison of the performances of GFRP-reinforced CRCP on various subbase types was simulated in this section. The linear bond-slip relationships between the concrete slabs and various subbase types, in terms of bond-slip stiffness per unit area of slab base (GPa/m (lbf/in^2/inch)), were utilized for the simulation; the relationships were obtained experimentally by a group of researchers at the University of Texas.[33,34,35] The subbase types considered are untreated clay, asphalt stabilized, flexible, lime-treated clay, and cement stabilized, listed in order of lowest to highest bond-slip stiffness/unit area (GPa/m (lbf/in^2/inch)). The value of bond-slip stiffness/unit area for each type is shown in table 7. In addition to the cases of the aforementioned subbase types, hypothetical bond-slip cases of 0.136, 0.271, 0.543, 1.357, and 2.715 GPa/m (500, 1,000, 2,000, 5,000, and 10,000 lbf/in^2/inch, respectively) were also simulated to find the appropriate range of bond-slip for the considered CRCP that eventually satisfies the limit of crack spacing, crack width, and the reinforcement stress level at crack. Granite aggregate concrete was used in this simulation based on material properties listed in table 5.

Table 7 and figure 65 show the predicted mean crack spacing and crack width over the bond-slip stiffness/unit area. It can be seen from figure 65 that the higher bond-slip results in smaller crack spacing, which in turn causes narrower crack widths. This result is reasonable since the higher bond-slip from the subbase provides the concrete slab with more restraint, causing higher tensile concrete stress under the concrete shrinkage and temperature drop and thus creating more cracks in a certain length of the slab.

Table 7. Mechanistic prediction of crack development and reinforcement tensile stress at crack for GFRP-CRCP (varied with different types of subbase).

Subbase Type[1]	Bond-Slip Stiffness/Unit Area ($lbf/in^2/inch$)	Mean Crack Spacing (ft)	Crack Width (inch)	Reinf. Tensile Stress at Crack (ksi)
Untreated clay	21.95	8.62	0.0478	28.501
Asphalt stabilized	55.88	6.94	0.0388	25.466
Flexible	145.45	6.94	0.0388	25.468
Lime-treated clay	154.55	6.76	0.0378	24.769
~	500	5.95	0.0334	23.255
~	1,000	5.68	0.0318	22.893
~	2,000	4.64	0.026	20.887
~	5,000	3.57	0.0201	18.256
~	10,000	2.91	0.0164	16.250
Cement stabilized	15,400	2.45	0.0139	14.871

[1]Granite aggregate is used for concrete mix; number 6 GFRP rebar is considered.
1 $lbf/in^2/inch$ = 0.271 MPa/m; 1 ft = 0.305 m; 1 inch = 25.4 mm; 1 ksi = 6.89 MPa

In the prediction, the asphalt-stabilized subbase results in a mean crack spacing of 2.115 m (6.94 ft) and a crack width of 0.99 mm (0.0388 inch); these results are on the verge of the upper limit. Therefore, the asphalt-stabilized subbase appears to approximately provide the minimum allowable bond-slip (15.169 MPa/m (55.88 $lbf/in^2/inch$)) necessary to avoid spalling distress of the given CRCP. The cement-stabilized subbase was found to have nearly the maximum allowable bond-slip, resulting in a mean crack spacing of 0.747 m (2.45 ft) and a crack width of 0.35 mm (0.0139 inch). The mean crack spacing for the cement-stabilized subbase is somewhat small compared with its limit of about 1.067 m (3.5 ft), having the possibility of punchout distress.

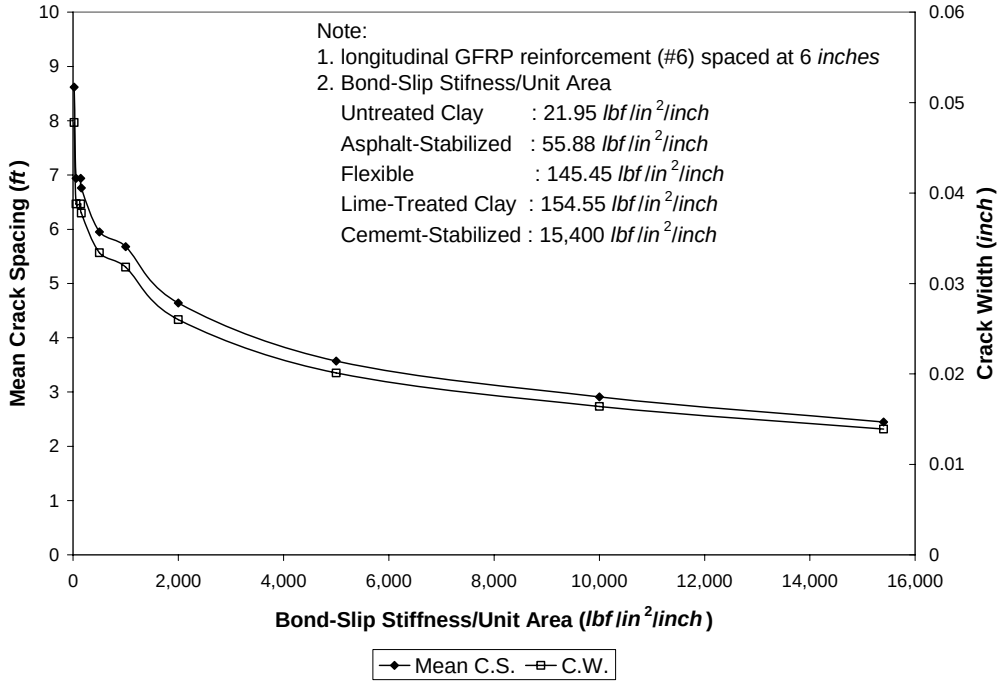

1 lbf/in^2/inch = 0.271 MPa/m; 1 ft = 0.305 m; 1 inch = 25.4 mm

Figure 65. Graph. Mean crack spacing and crack width versus bond-slip stiffness/unit area (ρ = 0.0074; granite aggregate concrete).

The tensile stresses in the GFRP reinforcement at cracks were also predicted over various subbase types (figure 66). As can be seen in the figure, higher bond-slip causes lower tensile stress in the reinforcement at the crack since the smaller crack spacing is expected with the higher bond-slip. The tensile stresses in the reinforcement corresponding to the subbase types range from about 103.43 to 199.96 MPa (15 to 29 ksi). The tensile stress levels for most subbase types, except for that of the cement-stabilized, exceed the allowable tensile stress of 124 MPa (18 ksi). The allowable tensile stress, as can be seen from the figure, is attained at a bond-slip of about 1.357 GPa/m (5,000 lbf/in^2/inch). Therefore, in order to avoid both spalling distress and early failure of GFRP reinforcement in the CRCP, the bond-slip should be held by at least 1.357 GPa/m (5,000 lbf/in^2/inch). Only the cement-stabilized subbase meets this criterion, even though it may have some possibility of causing punchout distress in the CRCP. In this simulation calculated by the CRCP8 program, the bond stress between the concrete and reinforcement leads to stress changes in the concrete and reinforcement, and the bond stress varies in the bond development zone; the location of this zone is determined by solving the system of governing equations with the assumed bond stress distribution function and the reinforcement boundary condition.[(3)]

The performance of the GFRP-CRCP design presumably proposed by FE analysis in chapter 5 was also mechanistically examined by CRCP8. Since the design was

established with the limestone concrete with a compressive strength, f_c', of 27.58 MPa (4,000 psi), the concrete material properties become a little different from those shown in table 6, which are based on f_c' = 31.03 MPa (4,500 psi). The concrete material properties of tensile strength, flexural strength, and drying shrinkage change to 2.37 MPa (344 psi), 3.83 MPa (556 psi), and 712 με, respectively. However, the CTE of 6.84 με/°C (3.8 με/°F) and Young's modulus of 24.8 GPa (3.6×10^6 lbf/in^2) are assumed to remain the same when f_c' = 27.58 MPa (4,000 lbf/in^2). The temperature input for the mechanistic exam also remains the same as that in table 6. This proposed GFRP-CRCP, which is designed utilizing a flexible subbase (or lime-treated clay subbase), is predicted to create a mean crack spacing of 1.466 m (4.81 ft), a crack width of 0.44 mm (0.0173 inch), and a reinforcement tensile stress at crack of 123.93 MPa (17.974 ksi). All of the results appear to be within their own limits and, therefore, the proposed GFRP-CRCP is expected to perform successfully.

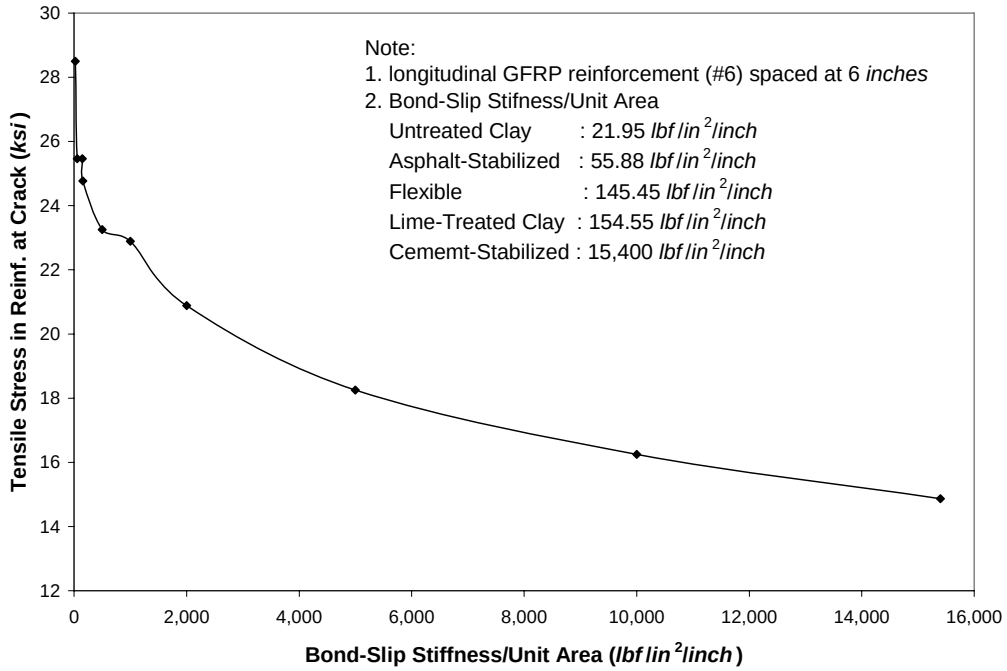

1 lbf/in^2/inch = 0.271 MPa/m; 1 ksi = 6.89 MPa; 1 inch = 25.4 mm

Figure 66. Graph. Tensile stress in GFRP reinforcement at crack versus bond-slip stiffness/unit area (ρ = 0.0074; granite aggregate concrete).

The performance of GFRP-CRCP in response to traffic loading is mainly dependent on the overall stiffness of the CRCP system. It is generally known that the flexural stiffness of the slab can be significantly influenced by the slab thickness rather than the reinforcement.[30] The thickness design, which determines the pavement stiffness, is accordingly dependent on load transfer coefficient, so it is currently thought that as long as the load transfer capability of GFRP-CRCP is satisfactory, the thickness of GFRP-CRCP may be able to remain the same, providing a pavement stiffness comparable to that

of steel-CRCP. [2] Currently, the thickness design procedure of steel-CRCP follows that of conventional jointed pavement, and the thickness of steel-CRCP is also recommended to be the same as that of conventional jointed pavement.[2,10] However, it is still necessary to investigate the performance of GFRP-CRCP in the field to verify this preliminary concept of GFRP-CRCP thickness design. In addition, it is noted that CRCP8 was designed for steel-CRCP with empirical data collected from the field with only steel-reinforced CRCPs. Hence, the GFRP-CRCP performance predicted from CRCP8 needs to be verified by monitoring of future construction of a GFRP-reinforced CRCP in the field. It is noted that the current AASHTO limiting criterion of 1 mm crack width is developed from the steel-reinforced CRCP. Field investigation report[36] of steel-reinforced CRCPs shows that high load transfer efficiency (LTE) (about 90%) is maintained for CRCPs at different ages, and the LTE is not influenced by the amount of reinforcement used (0.5% to 0.75%) or the crack spacings (0.5 to 2.5 m). Further research is needed to investigate the relationship between the crack width and its corresponding LTE of a GFRP-reinforced CRCP.

A possible future construction of 27.94-cm- (11-inch-) thick GFRP-reinforced and steel-reinforced CRCP sections are being planned in Elkins, West Virginia, in 2005. Under a given construction condition from the West Virginia Department of Transportation (WVDOT), using number 7 longitudinal GFRP rebars at 15.24-cm (6-inch) spacing on the line about 2.54 cm (1 inch) above the middepth of the slab is predicted to be an economically applicable design for GFRP-CRCP with limestone concrete on the asphalt-stabilized subbase. In addition, number 6 GFRP rebars spaced at 1.219 m (48 inches (4 ft)) will be installed as transverse reinforcement. For the steel-reinforced CRCP, number 6 longitudinal steel rebars spaced at 15.24 cm (6 inches) will be adopted on the same subbase along with number 5 transverse steel rebars spaced at 1.219 m (48 inches (4 ft)). After the construction, the field monitoring of both the CRCPs will be followed to compare and evaluate the performance of the GFRP-CRCP in terms of crack spacing, crack width, and the number of distresses (such as spalling and punchout).

CHAPTER 7. SUMMARY, CONCLUSIONS, AND RECOMMENDATIONS

SUMMARY AND CONCLUSIONS

In this report, the concrete stresses induced in a GFRP-reinforced concrete slab due to concrete shrinkage and temperature variations have been analytically calculated in comparison to those induced in a steel-reinforced concrete slab, and the validity of the analytical model has been verified numerically and experimentally. The analytical solution indicates that a low Young's modulus of GFRP rebar results in a stress reduction in concrete slabs. The thermal stress in concrete can be either tensile or compressive, depending on temperature variation and the CTEs of the concrete and the GFRP reinforcement used.

From comparison with the finite element calculation, the analytical solution of average axial concrete stresses is shown to be valid throughout the longitudinal (*x*-) direction, especially in the vicinity of the slab's middle section, where the maximum average axial stresses in concrete appeared. Meanwhile, the comparison also reveals the applicability of the FE method to the CRCP analysis. A 1.524-m (5-ft) CRCP segment FE model was built to simulate the behavior of the CRCP and to study the effects of CRCP design considerations (such as the CTE of concrete, the friction from the pavement's subbase, and the bond-slip between concrete and reinforcement) on stress development and crack width in the CRCP. It is shown that using concrete with a lower CTE reduces the concrete's tensile stress level when exposed to temperature drop, and a weaker bond between the concrete and reinforcement also decreases the concrete tensile stress level in the CRCP and the tensile reinforcement stress level at its cracks. With a higher subbase friction, the CRCP is more likely to crack from its bottom area since the concrete stress level at the bottom will be higher than that at the top. The results give ways to favorably control the larger crack spacing and wider cracks of the GFRP-reinforced CRCP caused by the GFRP's low elastic modulus; in order to satisfy the limiting criteria, with a given CTE of concrete, one can choose to (1) increase the amount of reinforcement, (2)increase the bond between concrete and reinforcement, and/or (3) increase the bond between concrete slab and subbase.

From the FE study, a feasible longitudinal reinforcement design of 25.4-cm- (10-inch-) thick GFRP-reinforced CRCP has been proposed for a given condition by evaluating concrete stress developments in the 1.067-m (3.5-ft), 1.524-m (5-ft), and 2.438-m- (8-ft-) long CRCP slab segments with limestone concrete. Using number 6 longitudinal GFRP rebars at 15.24-cm (6-in.) spacing at the middepth of the slab is shown to be an economically feasible design for GFRP-CRCP on the flexible subbase (or lime-treated clay subbase). In addition, number 5 GFRP rebars spaced at 1.219 m (48 inches (4 ft)) will be adequate as transverse reinforcement.

The mechanistic analysis program has been used to analyze the GFRP-CRCPs with different types of concrete coarse aggregate and subbase. Higher CTE, higher Young's modulus, lower tensile strength, and larger drying shrinkage of concrete appear to reduce

the crack spacing in the CRCP. However, even though the crack width is generally narrower as the crack spacing is smaller, it can open wider after the crack formation settles down. This occurs when ambient temperature and air humidity levels drop enough to cause large concrete volume change so that the crack width of those smaller crack spacing sections will become larger. Higher subbase friction always causes smaller crack spacing followed by narrower crack width. From the mechanistic analysis results, the GFRP-CRCPs with the limestone, sandstone, or siliceous river gravel concrete on asphalt-stabilized subbase seems to perform satisfactorily without raising the GFRP-reinforcement ratio under a given design condition provided by VDOT. In addition, the subbase that can provide a bond-slip of about 1.357 GPa/m (5,000 lbf/in^2/inch) is able to provide a satisfactory performance of the GFRP-CRCP with granite concrete.

Currently, the designs of a 27.94-cm- (11-inch-) thick GFRP-reinforced CRCP and a steel-reinforced CRCP section have been prepared and are waiting to be constructed in West Virginia in 2006.

RECOMMENDATIONS

- Further studies of the effect of a high transverse CTE of the GFRP rebar on its bond with concrete at various temperatures and on cracking in the GFRP-reinforced CRCP are necessary.

- Investigations into the effect due to the low transverse (shear) strength of the GFRP rebar on the load transfer at the cracks generated in the GFRP-reinforced CRCP should be conducted. Investigation of the relationship between the load transfer efficiency and the crack width is required.

- Developing the previously mentioned alternative reinforcement position for minimizing the amount of GFRP reinforcement needed while still favorably controlling the cracking in the GFRP-reinforced CRCP would be economically beneficial.

- Development of standard design guidelines to clearly specify the limiting criteria (such as crack spacing, crack width, and reinforcement stress level for the GFRP-reinforced CRCP) is needed. Currently, the AASHTO guideline for the steel-reinforced CRCP design can only serve as a reference.

ACKNOWLEDGMENTS

The authors acknowledge the assistance provided by the Constructed Facilities Center, West Virginia University (WVU), during this study. This report also constitutes part of Mr. Jeong-Hoon Choi's Ph.D. dissertation at WVU.

REFERENCES

1. Neff, T. L., and Ray, G. K., *CRCP Performance: An Evaluation of Continuously Reinforced Concrete Pavements in Six States*, Concrete Reinforcing Steel Institute, 1986.

2. AASHTO, *AASHTO Guide for Design of Pavement Structures*, American Association of State Highway and Transportation Officials, Washington, D.C., 1993.

3. Won, M.; Hankins, K.; and McCullough, B. F., "Mechanistic Analysis of Continuously Reinforced Concrete Pavements Considering Material Characteristics, Variability, and Fatigue," Research Report 1169-2, Center for Transportation Research, University of Texas at Austin, 1991.

4. Kim, S. M.; Won, M. C.; and McCullough, B. F., "CRCP-9: Improved Computer Program for Mechanistic Analysis of Continuously Reinforced Concrete Pavements," Research Report 1831-2, Center for Transportation Research, University of Texas at Austin, 2001.

5. Suh, Y. C.; Hankins, K.; and McCullough, B. F., "Early-Age Behavior of Continuously Reinforced Concrete Pavement and Calibration of the Failure Prediction Model in the CRCP-7 Program," Research Report 1244-3, Center for Transportation Research, University of Texas at Austin, 1992.

6. Zhang, J.; Li, V. C.; and Wu, C., "Influence of Reinforcing Bars on Shrinkage Stresses in Concrete Slabs," *ASCE Journal of Engineering Mechanics*, V. 126, No. 12, 2000, pp. 1297–1300.

7. Chen, H. L., and Choi, J. H., "Effects of GFRP Reinforcing Rebars on Shrinkage and Thermal Stresses in Concrete," *Proceedings of the 15th ASCE Engineering Mechanics Conference*, Columbia University, New York, NY, June 2002.

8. Choi, J. H., and Chen, H. L., "Design Considerations of GFRP-Reinforced CRCP," *Field Applications of FRP Reinforcement: Case Studies*, SP-215, S. Rizkalla, and A. Nanni, eds., American Concrete Institute, Farmington Hills, MI, 2003, pp. 139–158.

9. Chen, H. L., and Choi, J. H., "Effects of GFRP Reinforcing Rebars on Shrinkage and Thermal Stresses in Continuously Reinforced Concrete Pavement," submitted to *ACI Structural Journal*, 2004.

10. Huang, Y. H., *Pavement Analysis and Design*, Second Edition, Prentice Hall, Englewood Cliffs, NJ, 2004.

11. Tayabji, S. D.; Stephanos, P. J.; Gagnon, J. S.; and Zollinger, D. G., "Performance of Continuously Reinforced Concrete Pavements, Volume II: Field Investigations of CRC Pavements," Publication No. FHWA-RD-94-179, Federal Highway Administration, McLean, VA, 1998.

12. Sprinkel, M. M., Personal Communication, Virginia Transportation Research Council, Charlottesville, VA, 2002.

13. York, G. P., "Continuously Reinforced Concrete Pavement-The State of the Art," Technical Report No. AFWL-TR-71-102, Air Force Weapons Laboratory, 1971.

14. Zollinger, D. G., and Barenberg, E. J., "Field Investigation of Punchout Distress in Continuously Reinforced Concrete Pavement in Illinois," *Transportation Research Record*, No. 1286, Transportation Research Board, 1990, pp. 1–13.

15. Kim, S. M.; Nam, J. H.; and McCullough, B. F., "Sensitivity of Design Variables to Continuously Reinforced Concrete Pavement Behavior," *Proceedings of the 82nd Annual Meeting of the Transportation Research Board*, Paper No. 03-4204, Transportation Research Board of the National Academies, Washington D.C., January 2003.

16. CRSI, *CRCP in Texas: Five Decades of Experience*, Concrete Reinforcing Steel Institute, Schaumburg, IL, 2004.

17. Zollinger, D. G., and Barenberg, E. J., "Mechanistic Design Considerations for Punchout Distress in Continuously Reinforced Concrete Pavement," *Transportation Research Record*, No. 1286, Transportation Research Board, 1990, pp. 25–37.

18. Gharaibeh, N. G., and Darter, M. I., "Probabilistic Analysis of Highway Pavement Life for Illinois," *Proceedings of the 82nd Annual Meeting of the Transportation Research Board*, Paper No. 03-4294, Transportation Research Board of the National Academies, Washington D.C., January 2003.

19. PCA, *Thickness Design for Concrete Highway and Street Pavements*, Portland Cement Association, Skokie, IL, 1984.

20. CRSI, *Construction of Continuously Reinforced Concrete Pavements*, Concrete Reinforcing Steel Institute, Schaumburg, IL, 1983.

21. Dossey, T., and McCullough, B. F., "Characterization of Concrete Properties with Age," Research Report 1244-2, Center for Transportation Research, University of Texas at Austin, 1991.

22. Won, M. C.; Dossey, T.; Easley, S.; and Speer, J., *CRCP-8 Program User's Guide*, Center for Transportation Research, University of Texas at Austin, 1995.

23. Kim, S. M.; Won, M. C.; and McCullough, B. F., "CRCP-10 Computer Program User's Guide," Research Report 1831-4, Center for Transportation Research, University of Texas at Austin, 2001.

24. Mehta, P. K., and Monteiro, P. J. M., *Concrete: Structure, Properties and Materials*, Second Edition, Prentice Hall, Englewood Cliffs, NJ, 1993, 548 pp.

25. ACI Committee 222, *ACI 222R-01: Protection of Metals in Concrete against Corrosion*, American Concrete Institute, Farmington Hills, MI, 2001.

26. ACI Committee 440, *ACI 440.1R-03: Guide for the Design and Construction of Concrete Reinforced with FRP Bars*, American Concrete Institute, Farmington Hills, MI, 2003.

27. Cox, H. L., "The Elasticity and Strength of Paper and Other Fibrous Materials," *British Journal of Applied Physics*, V. 3, March 1952, pp. 72–79.

28. Mindess, S., and Young, J. F., *Concrete*, Prentice Hall, Englewood Cliffs, NJ, 1981, 499 pp.

29. Mosley, W. H., and Bungey, J. H., *Reinforced Concrete Design*, 4th Edition, Macmillan Education Ltd., London, U.K., 1990.

30. McCullough, B. F., *CRC-Highway Pave: Design of Continuously Reinforced Concrete Pavements for Highways*, PC Software Series, Concrete Reinforcing Steel Institute, Schaumburg, IL, 1993.

31. Finke, T. E., and Heberling, T. G., "Determination of Thermal-expansion Characteristics of Metals Using Strain Gages," *Experimental Mechanics*, SESA, April Issue, 1978, pp. 155–158.

32. Measurements Group, Inc., "Measurement of Thermal Expansion Coefficient Using Strain Gages," Tech Note TN-513-1, 1986.

33. Wesevich, J. W.; McCullough, B. F.; and Burns, N. H., "Stabilized Subbase Friction Study for Concrete Pavements," Research Report 459-1, Center for Transportation Research, University of Texas at Austin, 1987.

34. Wesevich, J. W., "Stabilized Subbase Friction Study for Concrete Pavements," Master Thesis, University of Texas at Austin, 1987.

35. Wimsatt, A. J., "Methods of Analyzing and Factors Influencing Frictional Effects of Subbases," Master Thesis, University of Texas at Austin, 1988.

36. Khazanovich, L. and Gotlif, A., "Evaluation of Joint and Crack Load Transfer Final Report," FHWA-RD-02-088, Federal Highway Administration, October 2003.